# An Experimental Apparatus for the Laser Cooling of Lithium and Rubidium

by

William James Bowden

Engineering Physics, The University of British Columbia, 2012

A THESIS SUBMITTED IN PARTIAL FULFILLMENT
OF THE REQUIREMENTS FOR THE DEGREE OF

**Master of Science**

in

THE FACULTY OF GRADUATE AND POSTDOCTORAL STUDIES
(Physics and Astronomy)

The University of British Columbia
(Vancouver)

October 2014

© William James Bowden, 2014

# Abstract

We demonstrate a two species effusive source and Zeeman slower for lithium 6 and rubidium 85. The fluxes produced by this slower allow for magneto-optical trap loading rates in excess of $10^8$ atoms per second for both species. A detailed model is developed to predict the emission properties of the effusive source along with the flux of cold atoms produced by the slower. Novel to this design is the mating of Zeeman slower magnetic field to the field produced by trapping coils which increases the effective length over which atoms are slowed. This allows for a smaller, more compact slower, without a sacrifice in performance. Details relating to the design and performance of the vacuum system and magnetic field producing coils are also covered. The apparatus can be easily adapted to operate with different atomic species making it well suited for ultracold atomic physics experiments studying mixtures or as starting point for the creation of hetero-nuclear molecules.

# Preface

This Master's thesis contains the result of research undertaken in the Quantum Degenerate Gases Laboratory under the supervision of Dr. Kirk Madison at the University of British Columbia. The laboratory is part of the Centre for Research in Ultra Cold Systems founded in 2008 and funded by a major grants from the Canada Foundation for Innovation and the British Columbia Knowledge Development Fund. This thesis focuses on the development of an experimental apparatus for the laser cooling of lithium and rubidium for the eventual study of ultra-cold mixtures and the creation of hetero-nuclear molecules. The laser systems and vacuum system used in Chapter 4 were built in collaboration with Janelle Van Dongen, Will Gunton, Kahan Dare, Steven Novakov, and Mariusz Semczuk. None of the text of the dissertation is taken directly from previously published or collaborative articles.

# Table of Contents

# List of Tables

# List of Figures

# Glossary

List of abbreviations used in this thesis.

| | |
|---|---|
| **AHC** | Anti-Helmholtz Configuration |
| **AOM** | Acousto-optic modulator |
| **CF** | ConFlat Vacuum Flange |
| **DAC** | Digital to Analog Converter |
| **HC** | Helmholtz Configuration |
| **LIRB** | Lithium Rubidium |
| **MOT** | Magneto-optical Trap |
| **NEG** | Non-evaporable getter |
| **RGA** | Residual Gas Analyzer |

# Acknowledgments

I entered my Master's thesis with the goal of focusing on a specific problem in physics culminating in me contributing in some meaningful way to society's general body of knowledge. During this time, I had the privilege of working with some remarkable people. In the end, I found these two parallel processes equally valuable and often thought it rather unfair that the former gets outlined in great detail in a 100 page thesis while the latter gets only a brief one page mention. However, I now realize that this is completely justified for if you were to ask me in the future "what was power of the MOT beam?" or "what is the ground state splitting of $^6$Li?" I would no doubt have to look it up, but if asked about the friendships I founded during these past two years I would be able to recall them instantly with great fondness.

First, I would like to acknowledge my supervisor, Dr. Kirk Madison, whose enthusiasm and insatiable curiosity for physics is truly inspiring. Under his guidance, I have acquired many technical skills as well as a scientific approach to thinking which will be invaluable throughout my professional career. Your dedication to your students is greatly appreciated.

I would like to thank the entire QDG group as the friendships I made with you all are one of the most valuable things gained from my work in the lab. In particular, I would like to acknowledge the two senior PhD students working on the project, Will Gunton and Mariusz Semczuk, for their guidance and teaching. Often their approach to experimental physics was as different as night and day (literally and figuratively), but through working with both I gained valuable experience and

insight into experimental physics research. I always enjoyed conversing with Mariusz about physics as if it was a sport and about baseball, with Will, as if it were a science.

I would like to thank Janelle Van Dongen for her patience in showing me the ins and outs of the lab when I first joined. I often told her that I would stop bothering her with my questions if she didn't always give me the answer, but she never would take my advice. I would also like thank Gene Polovy for our many fruitful engineering conversations which did wonders for teaching me things I thought I already knew. Finally, Kahan Dare and Komancy Yu, I would like to extend my appreciation for your constant willingness to lend a hand with whatever was causing me to pull my hair out on that given day. It always amazed me how quickly "my" problems were solved once they became "ours." Along with Kais Jooya, I look forward to following your future endeavors in the QDG lab.

I would like to extend my deepest thanks to my parents for their love and guidance. They instilled in me the curiosity and confidence to pursue my interest in physics. I commend your persistence in always asking how my day was only to be returned with an unenthusiastic fine.

Lastly, I would like to say thank you to Maggie Chao. I do not think I will ever be able to convey how much your support and love meant to me during these past two years.

# Chapter 1

# Introduction

## 1.1 Why Study Ultracold Polar Molecules?

The field of ultracold atomic physics focuses on the formation and control of ultracold atoms through which scientists can study a range of physical phenomena. These systems have been fruitful in improving our understanding of ultracold chemistry, few and many body physics, and quantum information theory. Such experiments are made possible by the arsenal of tools which have been developed to trap and cool various atomic species along with the ability to precisely control their internal and external degrees of freedom.

Building upon the success of ultracold atoms research, scientists are now looking for new systems to apply these same methods and further develop this toolkit. An excellent candidate for such work are ultracold molecules as their complex energy level structure, which includes rotational and vibrational levels, and long range interactions provide scientists with a handle through which they can manipulate these complex quantum systems. In particular, the inherent dipole moment of such molecules give rise to relatively strong, long range, dipole-dipole interactions which are easily tunable with external electric fields [1]. These interactions are of particular interest in the study of ultracold collisions between polar molecules as they give rise to novel types of resonances [2] and the potential to control chemical reactions [3]. These same tunable dipole-dipole interactions make ultracold molecules well suited for quantum information applications requiring the creation and manipulation of entangled states [4, 5]. Last but not least, the long range nature of these interactions, in contrast to the typical contact interactions found in other ultracold systems, could be utilized in quantum gases of polar molecules to study exotic phases of matter [6, 7].

Polar molecules made from lithium and rubidium are a promising candidate for such applications as they possess a predicted dipole moment of appropriately 4D in the $X(1)^1\Sigma_g^+$ ro-vibrational ground state [8]. However before such experiments can be conducted using ultracold Lithium Rubidium (LIRB) molecules, they must first be made.

## 1.2 Overview of Thesis

This thesis outlines the theory, design, construction, and characterization of an experimental apparatus used to produce large samples of cold $^{6}$Li, $^{85}$Rb, and $^{87}$Rb. The samples are held in a Magneto-optical Trap (MOT) and are a necessary starting point for the formation of ultracold LIRB molecules. The main focus of this thesis will be on a dual species Zeeman slower used to load the MOT and an analysis of its performance. This thesis is divided into three main parts covering the theory, design, and characterization of the experimental apparatus.

The theory chapter of the thesis focuses on the Zeeman slower and the effusive atomic sources. For the Zeeman slower, the principal of operation is covered with particular focus on slowing lithium and rubidium. With respect to the effusive sources, a model for accurately predicting the atomic flux, along with angular and velocity distribution is highlighted. The principal operation of a MOT is not covered as there exist numerous sources which present this information with excellent clarity and depth [9].

The design section of this thesis focuses on the design of the effusive sources, Zeeman slower, and experimental apparatus. The beginning of the chapter offers a review of existing Zeeman slower designs and insight into the various challenges of constructing a slower for multiple atomic species. The design of the effusive source for both rubidium and lithium is covered. The chapter ends with a discussion of the electronics used to control the Zeeman slower remotely and the design of the vacuum system.

The characterization section of the thesis starts with the investigation of the performance of the effusive sources along with a comparison of the theoretical model developed in Chapter 2. Next the performance of the Zeeman slower is characterized, first by spectroscopically probing the atomic beam to measure the modified velocity distribution and then by loading a MOT of both lithium and rubidium.

# Chapter 2

# Theory of Multi-species Atomic Source

## 2.1 Theory of Zeeman Slowers

The Zeeman slower was first developed by William Phillips in 1997 and uses the radiation pressure of light to slow atoms within an atomic beam. The ingenuity of the device is in its utilization of spatially varying magnetic fields that Zeeman shift the atomic levels to compensate for the changing Doppler shift as the atoms are slowed. Without compensation for the Doppler shift, after slowing by a few tens of meters per second, the atoms would no longer be in resonance with the slowing beam. However, by correcting for this shift, the Zeeman slower can slow beams from 1000 m/s to 10 m/s which makes them ideal for loading a MOT.

The scattering force, $F_s$, exerted on an atom moving with velocity $v$ towards a counter propagating laser beam with wavenumber $k$ and intensity $I = s_0 I_s$ [1], with $I_s$ being the saturation intensity of the atomic transition of natural width $\gamma$, is given by:

$$F_s = \frac{\hbar k \gamma}{2} \frac{s_0}{1 + s_0 + (2\delta'/\gamma)^2} \tag{2.1}$$

The effective detuning, $\delta'$, accounts for the following three sources of detuning: (1) laser detuning from the cycling transition frequency $\omega$ given by $\delta = \omega - ck$, (2) the Doppler detuning which is given by $kv$, and (3) the Zeeman shift due to a magnetic field $B$ given by $\mu_B/\hbar$ where $\mu$ is the magnetic moment of the transition. Combining these three effects gives the expression for $\delta'$:

$$\delta' = \delta + krv - \mu' B/\hbar \tag{2.2}$$

The maximum force is achieved when the effective detuning is zero and results in constant deceleration, $a$, given by:

$$a = a_{max} \frac{s0}{1 + s0} \tag{2.3}$$

where $a_{max}$ is the largest possible deceleration in the limit of infinite intensity. It is convention to write the deceleration as $a = \eta a_{max}$ where $\eta$ is a design parameter between zero and one which controls how aggressively the atoms are slowed.

[1] $s_0$ is a dimensionless quantity often referred to as the saturation parameter.

Larger values of $\eta$ lead to larger initial capture velocities, but require more intense slowing beams and decrease the allowable deviation from the ideal slowing field. Given that the effective detuning must always be zero, the ideal slowing field is easily calculated under the assumption of constant deceleration. Using kinematics, the positionally dependent velocity is given by:

$$v(z) = \sqrt{v_c^2 - 2az} \tag{2.4}$$

where $v_c$ is the initial velocity of the atomic beam which can be captured by the slower. Inserting this expression into Equation 2.2 and setting the detuning to zero gives the desired field parameter.

$$B(z) = \frac{\hbar k v_c}{\mu'} \sqrt{1 - \frac{2a}{v_c^2} z} - \frac{\hbar \delta}{\mu'} \tag{2.5}$$

Therefore, the desired field is uniquely defined by an amplitude $B_a$, length scale $z_0$, and finally an offset $B_0$ given by:

$$\begin{aligned} B_a &= \frac{\hbar k v_c}{\mu'} \\ z_0 &= \frac{v_c^2}{2\nu a_{max}} \\ B_0 &= \frac{\hbar \delta}{\mu'} \end{aligned} \tag{2.6}$$

and such, the desired field can be rewritten as:

$$B(z) = B_a \sqrt{1 - \frac{z}{z_0}} - B_0 \tag{2.7}$$

As an aside, it is now clear what effect $\eta$ has on the field profile; it effectively stretches the field allowing atoms to spend more time at a particular magnetic field to ensure they slow to the desired velocity at that position. Figure 2.1 shows the ideal field for a 50 cm slower with $\eta = .75$ for both $^6$Li and $^{85}$Rb.

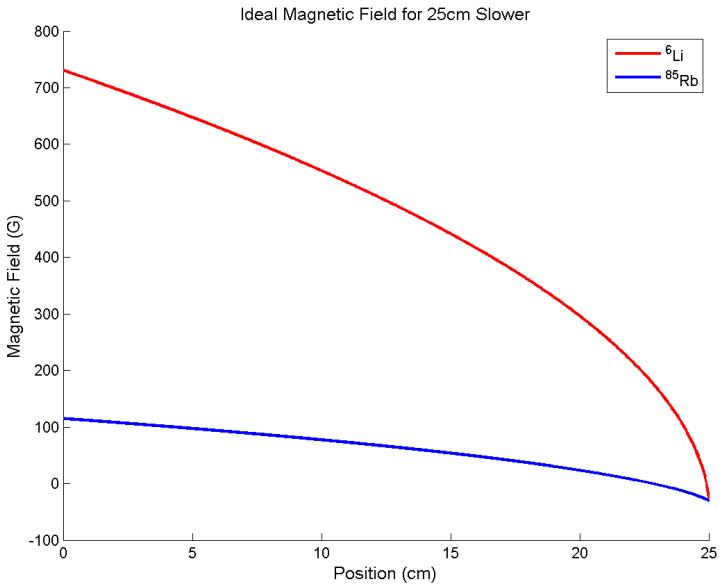


**Figure 2.1:** Ideal magnetic fields to slow $^6$Li and $^{85}$Rb.

### 2.1.1 The Zeeman Effect

In order to calculate the desired magnetic field profile, the dependence of energy eigenstates on an external magnetic field must be calculated. For typical magnetic field strength, the energy splitting is on the order or greater than the hyperfine structure, but much less than the fine structure. Therefore the relevant Hamiltonian is the one which takes into account both the effect of an external magnetic field and the coupling of the nucleus to the internal electric and magnetic fields which gives rise to the hyperfine structure. The hyperfine Hamiltonian including the magnetic dipole and electric quadrupole terms is given by:

$$H_{hfs} = A_{hfs}\mathbf{I}\cdot\mathbf{J} + B_{hfs}\frac{3(\mathbf{I}\cdot\mathbf{J})^2 + \frac{3}{2}\mathbf{I}\cdot\mathbf{J} - I(I+1)J(J+1)}{2I(2I-1)2J(2J-1)} \tag{2.8}$$

where $A_{hfs}$ and $B_{hfs}$ are the magnetic dipole and electric quadrupole constants, respectively and $J$ and $I$ are the total electronic angular momentum operator and the nuclear spin operator, respectively. Table 2.1 lists these values for the various species of interest in this thesis [10, 11].

**Table 2.1:** Hyperfine constants for $^6$Li, $^{85}$Rb, and $^{87}$Rb.

| Constant | Value [MHz] | Ref |
|---|---|---|
| $^6$Li $2^2S_{1/2}$ Magnetic Dipole | 152.1368407 | [12] |
| $^6$Li $2^2P_{3/2}$ Magnetic Dipole | -1.155 | [12] |
| $^6$Li $2^2P_{3/2}$ Electric Quadrupole | -0.10 | [12] |
| $^{85}$Rb $2^2S_{1/2}$ Magnetic Dipole | 1011.910813 | [12] |
| $^{85}$Rb $5^2P_{3/2}$ Magnetic Dipole | 25.0020 | [12, 13] |
| $^{85}$Rb $5^2P_{3/2}$ Electric Quadrupole | 25.790 | [12, 13] |

This coupling results in neither the projection of $J$ nor projection of $I$ being conserved quantities resulting in them being no longer good quantum numbers. However, this coupling still ensures that total angular momentum $F$, given by the sum of $I$ and $J$, and its projection $m_f$ remain conserved quantities. Hence, $F$ and its projection $m_F$ remain good quantum numbers and the above Hamiltonian is diagonalized in the $|I,J,F,m_F\rangle$ basis.

When a static magnetic field is applied, rotational symmetry is broken which lifts the degeneracy in $m_f$ values. The Hamiltonian which describes the interaction between an atom and the external field is given by:

$$H_B = \frac{\mu_B}{\hbar}(g_s\mathbf{S} + g_L\mathbf{L} + g_I\mathbf{I}) \cdot \mathbf{B} \tag{2.9}$$

where $g_S$ and $g_L$ are the g-factors for the electron's spin and orbit, while $g_I$ accounts for nuclear spin. The value for $g_s$ has been measured to a high degree of precision. The orbital g-factor to first order in the electron to nucleus mass ratio is:

$$g_L = 1 - \frac{m_e}{m_n} \tag{2.10}$$

The nuclear g-factor is challenging to calculate theoretically as it takes into account the complex structure of the nucleus and it is therefore best to use experimentally measured values. By convention, the magnetic field is taken to be along the z-axis. Making use of the fact the energy associated with the magnetic field within the Zeeman slower is weaker than the spin-orbit coupling, $J$ remains a good quantum number and $H_B$ can be written as:

$$H_B = \frac{\mu_B}{\hbar}(g_J J_z + g_I I_z)B_z \tag{2.11}$$

where $g_J$ is the Lande g-factor given by:

$$\begin{aligned} g_J = g_L \frac{J(J+1) - S(S+1) + L(L+1)}{2J(J+1)} \\ + g_s \frac{J(J+1) + S(S+1) - L(L+1)}{2J(J+1)} \end{aligned} \tag{2.12}$$

For calculating the slower field profile, a high degree of precision is not required and it is sufficient to neglect relativistic effects and mass corrections in which case $g_s = 2$ and $g_I = 1$ simplifying the above expression to:

$$g_J = 1 + \frac{J(J+1) + S(S+1) - L(L+1)}{2J(J+1)} \tag{2.13}$$

To calculate the energy spectrum the complete Hamiltonian, which includes both hyperfine and magnetic field effects, must be diagonalized. However, perturbation theory can be used to simplify this calculation in the two extremes when the $B \ll A_{hfs}/\mu_B$ and $B \gg A_{hfs}/\mu_B$. In the former case, $F$ and $m_F$ remain "pretty good" quantum numbers and the interaction Hamiltonian can be approximated:

$$H_B = \frac{\mu_B}{\hbar} g_F F_z B_z \tag{2.14}$$

where the hyperfine Lande g-factor is given by:

$$g_F = g_J \frac{F(F+1) - I(I+1) + J(J+1)}{2F(F+1)} + g_I \frac{F(F+1) + I(I+1) - J(J+1)}{2F(F+1)} \tag{2.15}$$

To first order in perturbation theory, the energy shift is linear in a magnetic field and depends only on the projection of $F$ onto the magnetic field axis and is given by:

$$\Delta E_{|I,J,F,m_F\rangle} = \mu_B g_F m_F B_z \tag{2.16}$$

In the other extreme, large fields cause $J$ and $I$ to process about the z-axis which leads to both $m_J$ and $m_I$ being conserved quantities and the effect of the hyperfine

Hamiltonian can be calculated via perturbation expansion in the $|J,I,m_J,m_I\rangle$ basis. In such a regime, first order perturbation gives the following energy spectrum:

$$\Delta E_{|I,J,m_J,m_I\rangle} = \mu_B(g_J m_J + g_I m_I)B + A_{hfs} m_I m_J + B_{hfs} \frac{9(m_I m_J)^2 - 3J(J+1)m_I^2 - 3I(I+1)m_J^2 + I(I+1)J(J+1)}{(4J(2J-1)I(2I-1))} \tag{2.17}$$

In the intermediate regime, the entire Hamiltonian must be diagonalized. This calculation is most easily done by first computing the two interaction terms in the Hamiltonian in their respective diagonal bases, i.e. $|J,I,F,m_F\rangle$ for the hyperfine term and $|J,I,m_J,m_I\rangle$ for the magnetic contribution. Next, either the hyperfine or magnetic component of the Hamiltonian is transformed to its non-diagonal basis using the Clebsh-Gordan coefficient which relates the two bases. The energy spectra are shown in the following figures along with the labeled slowing transition.

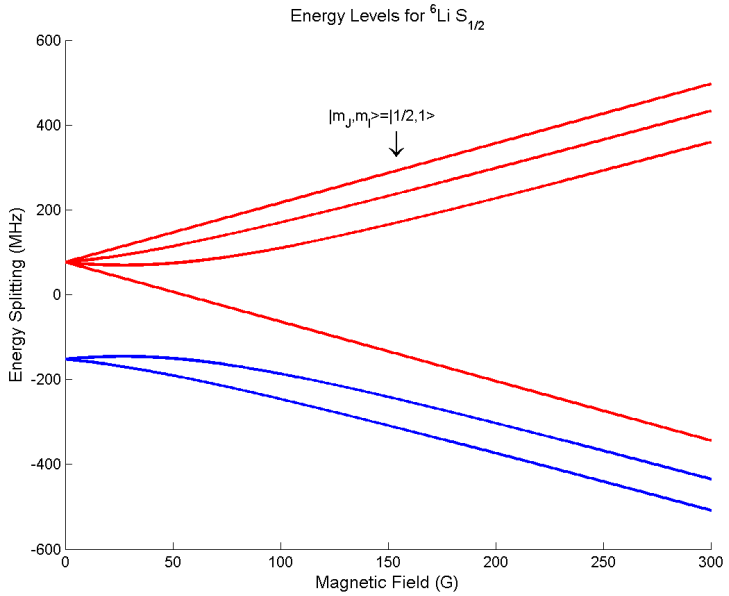


**Figure 2.2:** Hyperfine splitting of ground state of $^6$Li in a magnetic field. Colors correspond to different F states which are mixed by the external field.

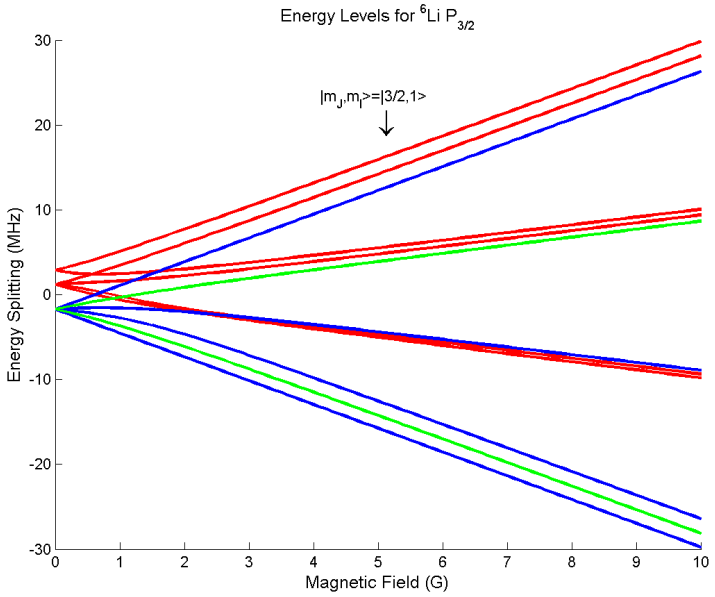


**Figure 2.3:** Hyperfine splitting of D2 manifold of $^6$Li in a magnetic field. Colors correspond to different F states which are mixed by the external field.

The stretched states experience a linear shift for all magnetic fields. This could have been deduced earlier as the Clebsh-Gordan which relates the maximal value of $m_F$ to maximal values of $m_I$ and $m_J$ is one. Therefore, the transition magnetic moment used in Equation 2.2 to calculate the desired field profile is:

$$\mu' = \mu_B(g_{F,e}m_{F,e} - g_{F,g}m_{F,g}) \tag{2.18}$$

where the subscript denotes the excited and ground state levels of the slowing transition. For $^{85}$Rb the slowing transition, in the low field basis, is from the $5^2S_{1/2}$ ($|J,I,F,m_F\rangle$=$|1/2,5/2,3,3\rangle$) level to the $5^2P_{3/2}$ ($|3/2,5/2,4,4\rangle$) level which has a transition moment from Equation 2.18 equal to simply $\mu_B$. For $^6$Li, the slowing transition is from the $2^2S_{1/2}$ ($|1/2,1,3/2,3/2\rangle$) level to the $2^2P_{3/2}$ ($|3/2,1,5/2,5/2\rangle$) level which has an transition of $\mu_B$ as well.

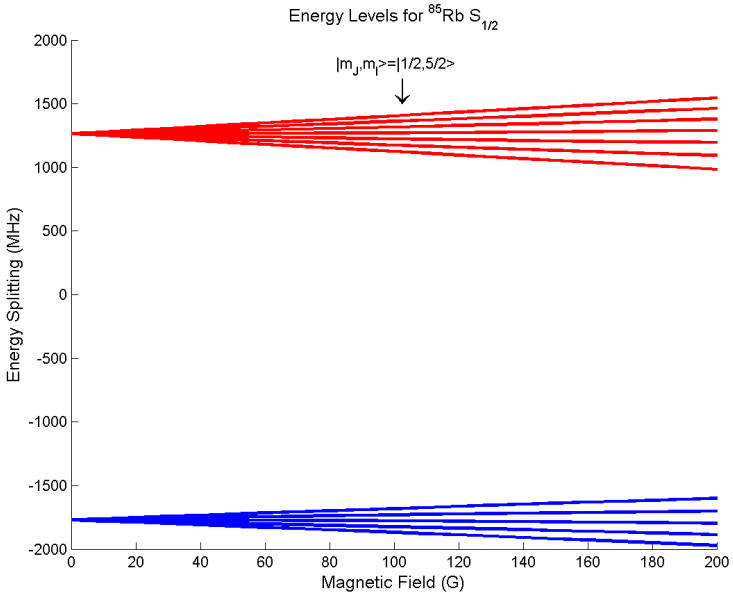


**Figure 2.4:** Hyperfine splitting of ground state of $^{85}$Rb in a magnetic field. Colors correspond to different F states which are mixed by the external field.

### 2.1.2 Alternative Field Profiles

The theoretical profile presented in Section 2.1 assumes that the energy splitting between the ground state and excited state increases with magnetic field. However, it is possible to design a Zeeman slower which operates on transitions for which the levels move closer in energy with increasing field. For such a slower, the required field must increase as the atom slows in order to compensate for the decreasing Doppler shift. The various types of Zeeman slower are often referred to by the polarization of light which drives the transition, namely $\sigma+$, $\sigma-$, and finally spin-flip. The major advantages and disadvantages of each type of slower are outlined is this section.

#### $\sigma$ + Zeeman Slower

In such a slower, atoms enter in a high field region which decreases as they slow. As a result of the atoms being in a low field when moving the slowest, only

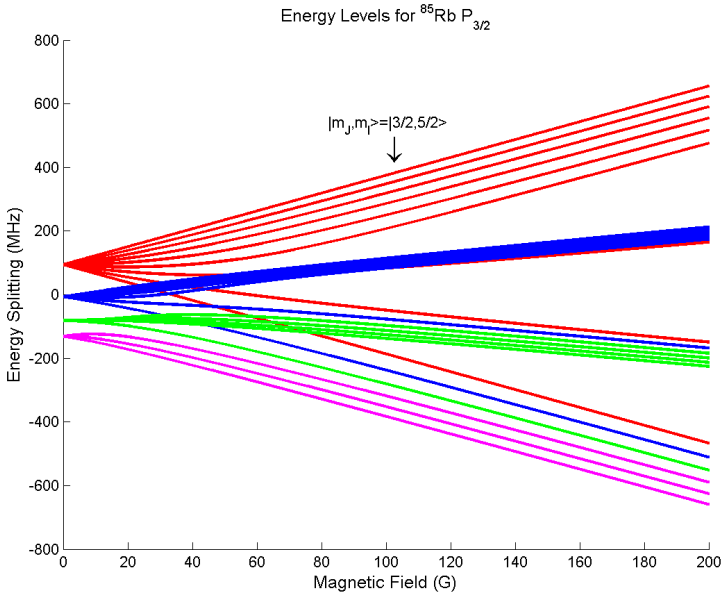


**Figure 2.5:** Hyperfine splitting of D2 manifold of $^{85}$Rb in a magnetic field. Colors correspond to different F states which are mixed by the external field.

a small detuning from the zero velocity resonance is needed to maintain the resonance condition. This is convenient as such detuning can be derived from existing MOT beams using an Acousto-optic modulator (AOM). However, having a near resonance slowing beam can interfere with the MOT. The small detuning leads to another disadvantage as the atoms can be stopped completely by the slowing beam before even reaching the MOT.

### $\sigma$ - Zeeman Slower

Opposite to the $\sigma+$ design, the atoms experience an increasing field as they move down the slower and experience the largest Zeeman shift at the end. As a result, such a design requires a large laser detuning, typically on the order of GHz, in order to keep the atom in resonance. Such a detuning is beneficial as it will have little influence on the behavior of the MOT, although practically it typically requires a more complicated scheme than simply frequency shifting the MOT lasers with an

AOM. The other benefit of having the field maximum at the end of the slower is that it ensures the atoms will quickly fall out of resonance with the slowing beam which prevents them from being further slowed and potentially stopped completely before reaching the MOT.

#### Spin-Flips Zeeman Slower

The final field profile commonly implemented has zero crossing at some point along the slower. The field can either be increasing or decreasing as is the case with the $\sigma+$ and $\sigma-$slowers, respectively, but the the detuning is changed to shift the field downwards. Practically, such a slower has a smaller absolute field maximum and therefore less current is needed to generate the desired profile which in turn leads to less heating. The atoms leave the slower at a larger field which requires greater detuning and therefore it shares many of the same benefits as the $\sigma-$ design. However, one drawback of the spin-flip design is that the atoms spend more time at smaller fields. In such a regime, the energy levels are closer spaced and the slower transitions are not closed. This leads to atoms getting optically pumped to dark states which stop the slowing process and requires additional beams to transfer atoms back into the slowing state. However, for some atomic species repump lasers are also needed for $\sigma+$ and $\sigma-$ designs as well.

### 2.1.3 Further Design Considerations

There are many key design considerations when determining the various features of the Zeeman slower. This subsection highlights a few key points which should be considered during the design process.

#### Adiabatic Slowing Condition

As mentioned in Section 2.1, there is a maximum deceleration imposed by the finite scattering rate. This limit constrains the maximum magnetic field gradient along the slower axes above which will no longer slow atoms. Given that the acceleration can be written as $a = v\frac{dv}{dz}$, differentiating Equation 2.2 leads to the expression for the maximum field gradient:

$$|\frac{dB(z)}{dz}| \ll \frac{\hbar k a_{max}}{\mu v(z)} \tag{2.19}$$

This criteria is typically referred to as the adiabatic slowing condition. Zeeman slowers are designed to slow at some constant fraction of $a_{max}$. However, this is not an optimal design strategy in terms of capturing the largest fraction of atoms for fixed slower length. The maximum gradient is inversely proportional to velocity which makes the adiabatic condition more stringent for faster moving atoms. Therefore, the strategy of uniformly stretching the field by changing $\eta$ is not ideal, rather it is better to vary $\eta$ depending on velocity at that particular location in the slower.

An alternative design strategy was proposed that takes into account the velocity dependence in the adiabatic slowing condition [14]. The design method defines a fixed difference, $\alpha$, between the gradient at a particular location and the maximum gradient defined in Equation 2.19 given the velocity at that position. Furthermore, both the Doppler shift and Zeeman shift are linear in velocity and magnetic field, respectively. In order for the two to cancel each other the $v(z)$ must be proportional to $B(z)$ with the proportionality factor being $\hbar k/\mu$. Hence, $v(z)$ can be written in terms of the magnetic field which transforms Equation 2.19 into the following differential equation:

$$\alpha = \frac{\hbar k a_{max}}{\mu' B} \pm \frac{\mu'}{\hbar k}\frac{\partial B}{\partial z} \tag{2.20}$$

The $\pm$ factor corresponds to whether the slower is $\sigma+$ or $\sigma-$. The factor $\alpha$ is referred to as the noise parameter and takes into account laser intensity fluctuations, current noise which produces the field fluctuations, or deviations in the magnetic field from the ideal profile due to winding. The differential equation is solved by using the Lambert W function and has the following solution:

$$B(z) = \frac{\hbar k}{\mu'}\frac{a_{max}}{\alpha}(W[(\frac{v_c\alpha}{a_{max}} - 1)\exp(\frac{z\alpha^2 + v_c\alpha}{a_{max}} - 1)] + 1) \tag{2.21}$$

where $v_c$ is the initial capture velocity of the slower. The value for $\eta$ when the atoms first enter the slower gives the corresponding value for alpha:

$$\alpha = (1-\eta)\frac{a_{max}}{v_i} \tag{2.22}$$

In the limit of $\alpha$ goes to zero, the above expression reduces to the one previously derived in Equation 2.7 by setting $\eta = 1$. For comparison, the capture velocity for a 50 cm slower for $^6$Li with a $\eta = 0.5$ and final velocity of 50 m/s would increase from 950 m/s to 1100 m/s and for $^{85}$Rb it increases from 240 m/s 270 m/s. These are improvements of approximately 15% which may not appear significant, but it should improve the loading by more than 50% given the $v^4$ scaling which will be derived in Section 2.1.4. Figure 2.6 shows the resulting fields from the two different design methods: the red curve is derived from Equation 2.7 which tunes the field using $\eta$ and the blue curve is Equation 2.21 which uses $\alpha$ as a design parameter.

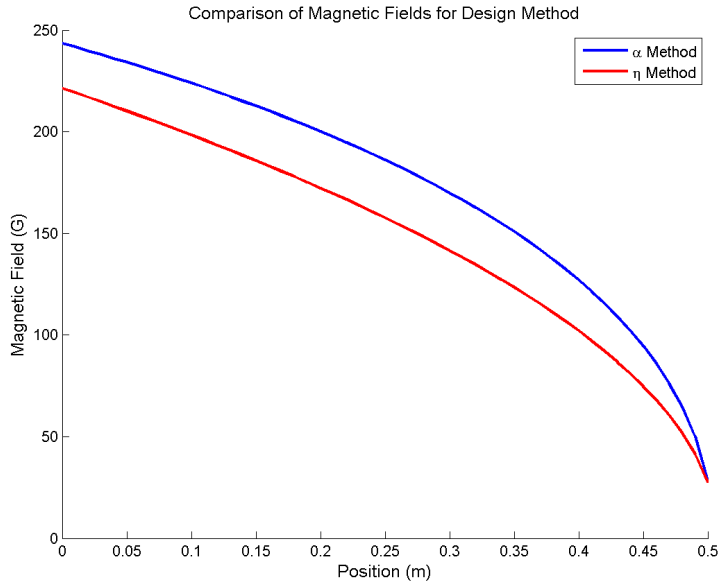


**Figure 2.6:** Comparison of a Zeeman slower for $^{85}Rb$ using the old design method utilizing $\eta$ as a design parameter and the new method using $\alpha$ . For fast moving atoms, the field gradients are the same for both methods, but the blue curve becomes steeper as the atoms slow down. The larger initial magnetic field leads to a larger capture velocity.

**Zeeman Slower for Multi-species**

The design of a multi-species slower requires different approaches depending on which combination of species is being slowed. Two questions must be addressed when designing a multi-species slower: (1) can the slower simultaneously slow the desired species when operating at the same magnetic field and (2) can the slower slow the different species when operating at different magnetic fields. Depending on the species being slowed, the answer to the first question is maybe, but fortunately the answer to the second question for all commonly slowed species is yes.

As derived in Section 2.1, the slowing profile is specified by the amplitude $B_a$ and a length scale $z_0$. The amplitude can be controlled via the current, but $z_0$ depends on the construction of the slower and cannot be easily changed in most designs. The value of $z_0$ is critical to the slower's operation as it controls $\eta$. It can be shown that if the final velocity is small compared to the initial velocity, which is always the case, then $z_0$ is a constant for all species. Let $z_{0,1}$ and $z_{0,2}$ be the slower length scale factors for atomic species 1 and 2. The ratio of these lengths, which can be taken to be greater than one without loss of generality, is given by Equation 2.6 as:

$$\frac{z_{0,1}}{z_{0,2}} = \frac{1+\frac{v_f^2}{2a_1 z}}{1+\frac{v_f^2}{2a_2 z}} \tag{2.23}$$

where $z$ is the slower length, $a$ is the deceleration, and it is assumed that both species have comparable final velocities. The quantity $2az$ is approximately the square of the initial capture velocity of the slower, $v_c$, and the above expression is:

$$\frac{z_{0,1}}{z_{0,2}} \approx 1+\frac{v_f^2}{2z}\frac{a_1-a_2}{a_1 a_2} < 1+\frac{v_f^2}{2za_1} \approx 1+\frac{v_f^2}{v_{c,1}^2} \tag{2.24}$$

For any effective Zeeman slower, the ratio of the final velocity to the initial velocity is greater than 10 which makes the largest difference between $z_0$ values less than one percent. Hence, if the Zeeman slower is designed for one species it can be used to slow any another atomic species by simply changing the amplitude $B_a$, most likely by increasing the current through the windings. In order to determine if a slower can effectively slow two species simultaneously one can look at the ratio

of $\eta$ which should be on the order of 1. Given that $B_a$ and $z_0$ are the same for both species, the ratio of $\eta_1$ to $\eta_2$ is given by:

$$\frac{\eta_1}{\eta_2} = \frac{M_1 \mu_1' k_2 \gamma_2}{M_2 \mu_2' k_1 \gamma_1} \tag{2.25}$$

For $^6$Li and $^{85}$Rb, this ratio is 0.04 due to large mass imbalance which eliminates the possibility for simultaneous slowing. A complete table showing this ratio for most trappable elements can be found in [15].

### 2.1.4 Optimal Zeeman Slower Length

Arguably the most critical design choice when constructing a Zeeman slower is deciding upon the length which in turn determines the maximal velocity which can be slowed. However, increasing the length may not actually increase the size of the MOT as the divergence of the beam leads to a flux which decreases in accordance with the inverse square law. The capture velocity, $v_c$ of a Zeeman slower of length $L$ is given by $\sqrt{2\eta a_{max} L}$ and the fraction of atoms captured is the integral of the velocity distribution function up to this capture velocity. For small velocities, the distribution function grows as $v^3$ and the integral grows as $v_c^4$. Therefore the flux, $\Phi$ is independent of the Zeeman slower length as:

$$\Phi \propto \frac{v_c^4}{L^2} \propto \frac{\sqrt{L}^4}{L^2} \tag{2.26}$$

This reasoning greatly oversimplifies the problem as it neglects that atoms do not travel in straight trajectories as they are slowed leading to a faster divergence and that the velocity distribution does not grow as $v^3$ indefinitely. Both of these factors motivate going to shorter slowers and begs the questions why have a slower at all? In practice, it is not desirable to have an atomic source in close proximity to the MOT as it limits achievable background pressure. When the atomic source is placed near the MOT and initially heated, the flux of alkali atoms increases. At low temperatures, background pressure typically stays unchanged as it is dominated by other sources rather than the outgassing of the oven. The MOT loading rate (i.e. the capturable flux) increases along with the steady state captured atom number with increasing temperature. Once the oven temperature is high enough that the out-

gassing of the source starts to dominant the background pressure, the atoms decay rate from the MOT increases. The steady state atom number, given by the ratio of the loading rate to the loss rate, would then be expected to saturate with increasing temperature as both rates are proportional to the atomic density inside the oven. However, this has not been observed with our previous experiential apparatus. Instead, the outgassing of the oven is primarily dominated by hydrogen or other gases that have a lower binding energy to the material and thus the MOT loss rate due to background gas collisions increases faster than the loading rate due to the flux of alkali atoms. This results in a maximum in the steady state MOT atom number with increasing oven temperature. [16, 17]. The Zeeman slower provides differential pumping which isolates the source section of the experimental apparatus from the science section and allows for lower background pressure without greatly reducing the flux.

## 2.2 Theory of Effusive Sources

The majority of cold atom experiments start with an effusive source which consists of a container containing a solid sample of the atomic species being investigated. The container has a small orifice through which atoms can leave. The flux of atoms leaving the source is controlled by heating the sample to increase or decrease the vapor pressure. In the molecular flow regime, the flux from a reservoir through a orifice channel is characterized by its Knudsen number, defined as the ratio between the mean free path length ($\lambda$) of atoms in the reservoir to the relevant transverse dimension of the orifice, e.g. the radius for a cylindrical hole. Effusive flow or molecular flow occurs when the Knudsen number is much larger than one. In this regime, the flux is proportional to the vapor pressure inside the reservoir. If the mean free path decreases below the channel radius, the flow transitions to a viscous or super-sonic flow characterized by a rapid increase in flux, quickly exhausting the source material. Furthermore, in the viscous regime there is a depletion of the low velocity tail of the Maxwell-Boltzmann Distribution [18]. The other relevant dimension is the channel length. For channels shorter than the mean free path, the channel is characterized as transparent. The angular distribution of the flux from the channel is comprised of a sharp peak confined to the region which

has direct line of sight into the reservoir and background flux due to diffusion from the channel walls. The other regime, when the mean free path is less than the channel length, is referred to as opaque flow. In this regime, inter-channel collisions change both the angular and velocity distribution of the atomic flux.

### 2.2.1 Transparent Regime

For an effusive source, the most relevant quantity of interest is the total number of atoms leaving the source, $N$, and the angular distribution in which they leave. The angular distribution is described by an intensity function, $I(\theta)$, which has units of atom per steradian per second. The angle $\theta$ is the angle from the normal of the exit channel opening. I assume the opening is circular and the angular distribution is rotationally symmetric. The total flux and the intensity are related by:

$$N = \int_{\Omega} I(\theta) d\Omega \tag{2.27}$$

The simplest transparent effusive source to model is an infinitely thin walled aperture. Such a source is often referred to as a cosine emitter as the angular distribution function is simply $\cos(\theta)$. Such an emitter is analogous to Lambert's cosine law in optics which states that the radiance from an ideal diffusive surface is proportional to the cosine of the viewing angle. The number of particles, $dN$, emitted into a solid angle in the direction defined by the angle $\theta$ from a reservoir of atoms with density $n$ and average velocity $\bar{v}$ through an aperture of area $A$ is given by [19].

$$dN = (\frac{d\Omega}{4\pi}) n\bar{v}\cos\theta A \tag{2.28}$$

Integrating the above expression from $\theta$ equal zero to $\pi/2$, an expression for the total flux from the cosine emitter is found:

$$N = (\frac{1}{4}) n\bar{v}A \tag{2.29}$$

The velocity distribution inside the oven is the standard Maxwell-Boltzmann Distribution ($F_{MB}^{3D}(v)$) for an ideal gas which is proportional to the velocity squared.

$$F_{MB}^{3D}(v) = \frac{4\pi v^2}{(\alpha\pi)^{3/2}} \exp -(\frac{v}{\alpha})^2 \tag{2.30}$$

where $\alpha$ is the standard expression for the most probable speed $\sqrt{2kT/m}$ [19]. However, this is not the distribution for the beam as the probability of an atom leaving the oven is proportional to its velocity. Simply put, faster moving atoms have a higher probability of leaving the oven per unit time and the velocity distribution inside the beam is given by:

$$F_{MB}^{Beam}(v) = \frac{2v^3}{\alpha^4} \exp -(\frac{v}{\alpha})^2 \tag{2.31}$$

The pre-factor can be derived given the normalization condition. If we consider a more realistic case for a finite length channel, the total flow is reduced by the Clausing factor, $W$, which accounts for the fact that wall collisions lead to a fraction of the atoms returning to the source. This effect alters the angular distribution resulting in it being described by a new distribution function, typically written as $\kappa f(\theta)$[20]. The number of particles emitted into a solid angle in a direction $\theta$ is now:

$$dN = \frac{d\Omega}{4\pi} W n \bar{v} \kappa f(\theta) A \tag{2.32}$$

For a circular channel with radius $a$ and length $L$, the Clausing Factor is given by[21]:

$$W = \frac{8a}{3L}(1 + \frac{8a}{3L})^{-1} \tag{2.33}$$

The variable $\kappa$ is referred to as the peaking factor and describes the ability of a specific channel geometry to focus the beam. It is defined as the ratio of the center line directional intensity ($I(\theta = 0)$) to the total flux $N$.

$$\kappa = \pi \frac{I(0)}{N} \tag{2.34}$$

The factor of $\pi$ is simply from convention such that the peaking factor for cosine emitter is one. Since the center line intensity is unchanged in the transparent regime, it follows that the peaking factor for a transparent channel is simply the in-

verse of the Clausing Factor. Unfortunately, the nomenclature for effusive sources varies significantly from reference to reference. I will follow the convention of Beijerinck and Verster and define the angular distribution as the product of the peaking factor and the angular profile, $f(\theta)$, which has the following normalization integral over the entire solid angle [20]:

$$\int_{\Omega} \kappa f(\theta) d\Omega = \pi \tag{2.35}$$

For long channels which provide a high degree of focusing ($L/a > 10$), the angular distribution function can be reasonably approximated. For angles which have direct line of sight into the oven ($\theta < \arctan(2a/L)$) the angular distribution is [20, 21]:

$$\kappa f(\theta) = \frac{2\cos\theta}{\pi W}[(1-W/2)R(p) + \frac{2}{3}(1-W) \times \frac{1-(1-p^2)^{3/2}}{p} + \frac{\pi W}{4}] \tag{2.36}$$

The values of of $p$ and $R(p)$ are defined as:

$$p = \frac{L\tan\theta}{2a} \tag{2.37}$$

$$R(p) = \arccos p - p(1-p^2)^{1/2} \tag{2.38}$$

For angles which do not directly extend into the reservoir the atoms observed are emitted from the walls and the distribution function is:

$$\kappa f(\theta) = \frac{8a\cos^2\theta}{\pi W \sin\theta}(1-W) + \frac{\cos\theta}{2} \tag{2.39}$$

Figure 2.7 shows the angular distributions for various peaking geometries multiplied by the Clausing factor. In all cases, the centerline intensity is the same. The velocity distribution leaving channel is identical to that of a cosine emitter as the atoms which fly directly from the interior and those which are emitted from the walls are in thermal equilibrium.

The key assumption in this derivation is atomic collision with the wall will result in the atoms being re-emitted in a random direction whose distribution is governed by the cosine law. Secondly, collisions within the channel are neglected.

If surface diffusion occurs such as wicking though the channel, the angular distribution will differ from that predicted above.

### 2.2.2 Opaque Regime

The opaque regime applies to the situation when the mean free path is less than the length of the channel, but still much larger than the diameter, and inter-molecular collisions within the tube modify the angular profile and velocity distribution. Determining these two profiles is challenging and an initial ansazt of the density profile along the length of the channel must be made [22]. If the channel is long, the density varies linearly from the source density, $n_0$, to the exit and any perturbation induced from the channel opening and exit can be neglected. It is convenient to assume the exit density is close to zero. Therefore, the density as a function position from the exit is $x\frac{n_0}{L}$. Using this density profile, the point in the channel at which the mean free path is equal to the remaining length of the channel can be found. This remaining length in the channel is denoted as $L'$ and can be calculated by setting the mean free path at a position $L'$ equal to $L'$ as follows [20, 22]:

$$\begin{aligned} \lambda[L'] &= \frac{1}{\sqrt{(}2)n(L')\pi\sigma} = L' \\ &= \frac{L}{\sqrt{(}2)n_0 L'\pi\sigma} = L' \Rightarrow L' = L\sqrt{Kn} \end{aligned} \tag{2.40}$$

where $K_n$ is also a Knudsen number, but it is now the ratio of the mean free path in the reservoir to the channel length, and $\sigma$ is the collisional cross section. The source density, $n'$ at the point $L'$ is given by:

$$n' = n_0\sqrt{K_n} \tag{2.41}$$

If we now make the simplifying assumption that the opaque channel behaves as a transparent channel with an effective length $L'$ and source density $n'$, we can treat the problem exactly as we did before for the transparent case. From this assumption, we can define the peaking factor for an opaque channel:

$$\kappa_{opaque} = \kappa_{trans}\sqrt{K_n} \tag{2.42}$$

This model will lead to underestimates of the total flux which results from the assumption of an isotropic velocity distribution at the distance $L'$. However, the channel length prior to $L'$ will help to focus the beam and provide a net velocity in the forward direction. On the other hand, if the channel was treated as transparent the resulting flux would be over estimated. Therefore, modeling the channel using both the actual length and the effective length will provide upper and lower bounds on the total flux. The lithium effusive source operates well within the transparent regime as the mean free path is on the order of meters. However, rubidium has a mean free path of about of 1 cm at 120°C which is approaching the opaque regime and should be considered when modeling the source.

### 2.2.3 Velocity Distribution in the Opaque Regime

The collisions within the channel lead to a modification in the velocity profile, in particular slow moving molecules experience a larger collisional rate and are depleted from the population. This is particularly concerning as the low velocity atoms which are trapped by the MOT. The mean free path within the channel depends on the density at that location and the atom's speed. An atom at position x away from the exit of the tube, will escape without any collisions with a probability given by:

$$P(x) = \exp[-\int_x^0 \frac{dx'}{\lambda(x')}] \tag{2.43}$$

Given the assumption of the linear density profile, the mean free path is proportional to the reciprocal of distance down the channel and the integral can be evaluated directly and the result is [23]:

$$P(x) = \exp[-\frac{(x/L)^2}{2K_n}] \tag{2.44}$$

It is now important to modify the mean free path to account for the dependence on velocity. In actuality, we should have done this earlier when we derived the angular profile of the opaque channel which would have resulted in a velocity dependent

effect length. However, for practical purposes this can be neglected as experimental results are in good agreement with the results derived previously. The velocity dependent mean free path length written in terms of the normalized speed $z$ defined as $v/\alpha$ is:

$$\lambda(z,x) = \frac{\lambda(x)}{\psi(z)} \tag{2.45}$$

where $\psi(z)$ is given by the following equation for which a derivation can be found in [24]:

$$\psi(z) = \frac{z\exp[-z^2] + \sqrt{\pi}(2+z^2)\mathrm{erf}(z)}{\sqrt{2\pi}z^2} \tag{2.46}$$

The rate at which molecules moving at a reduced speed $z$ at a position $x$ collide with a background gas with density $n(x)$ is the reciprocal of the mean free path multiplied by the particle's velocity. The number of particles in this reduced speed range is $n(x)F(z)dz$ where $F(z)$ is the velocity distribution. As a first approximation, we can assume collisions do not perturb the distribution significantly away from a Maxwell-Boltzmann distribution and will remain a valid estimator of $F(z)$. In accordance with the principle of detailed balance, the fraction atoms between $z$ and $z+dz$ entering into collisions must equal the number of molecules in the same velocity range produced by collisions. Hence, the number of molecules being produced due to collisions with velocity in range $z+dz$ in a channel volume $\pi a^2 dx$ is given by $\alpha z\lambda^{-1}(x)F(z)n(x)\pi a^2 dx$. Of these molecules, a fraction $1/4\pi$ is emitted into the solid angle along the tube axis. Of those molecules which are scattered in the forward direction along the tube axis a fraction will escape with the probability:

$$P(x) = \exp[-\psi(z)\frac{(x/L)^2}{2K_n}] \tag{2.47}$$

We can then integrate over the entire channel length to get the molecules which are emitted along the channel axis due to collisions. We also have to add the fraction that are emitted directly from the reservoir and make it to the exit without any collisions. This calculation was carried out in reference [23] and the resulting velocity distribution is given in terms of a perturbation function $P[K_n, Z]$:

$$F(z) \propto F_{MB}^{Beam}(z) P[K_n, Z] \tag{2.48}$$

The perturbation function depends on speed and channel geometry and is given by [23]:

$$P[K_n, z] = \frac{\pi}{2} \frac{\text{erf}[\sqrt{\psi(z)/2K_n}]}{\sqrt{\psi(z)/2K_n}} \tag{2.49}$$

To normalize the result, the above expression must be divided by integral over all velocities. Unfortunately, to the best of my knowledge this integral cannot be solved exactly, but can be easily computed numerically. As the channel length goes to zero, the perturbation function goes to 1 as expected. For large channel lengths, the contribution from molecules emitted directly from the reservoir goes to zero and the result no longer depends on the channel geometry. As a result, the function goes to a constant. Figure 2.8 shows the modified velocity profile. The effect is marginal and will be challenging to observe experimentally.

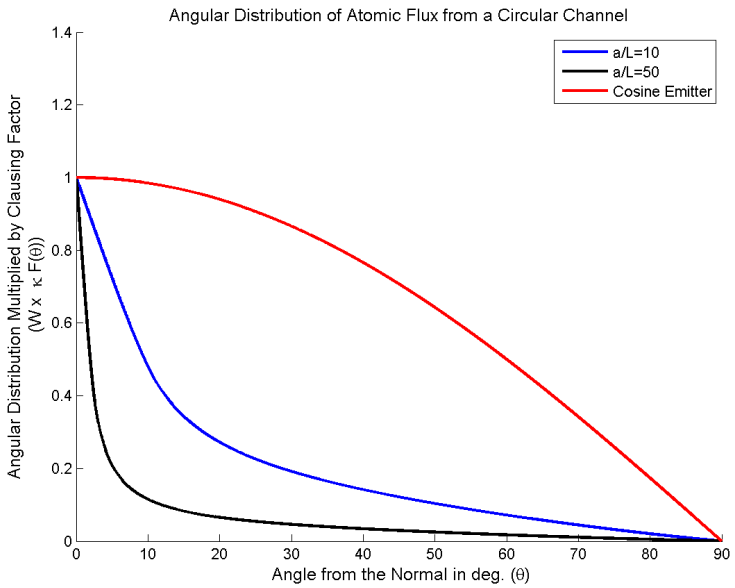


**Figure 2.7:** Angular distribution for an ideal cosine emitter compared to channels with an aspect ratio of aspect ratio of 10 and 50.

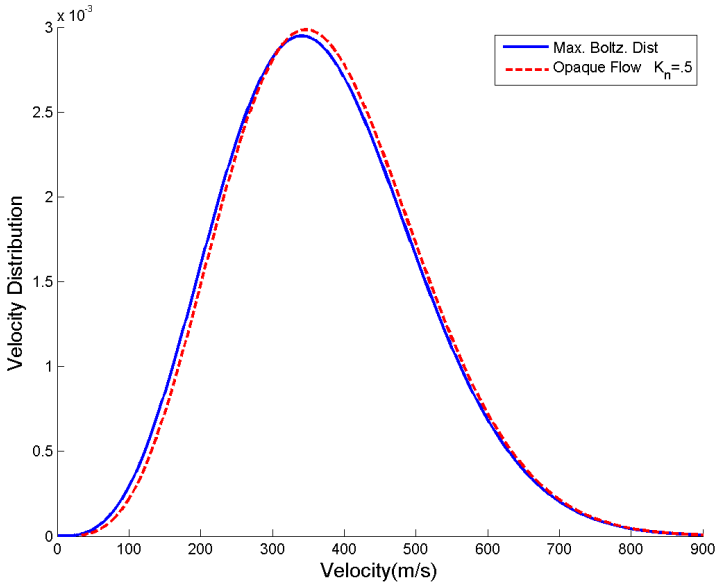


**Figure 2.8:** Velocity distribution from a transparent channel (Max. Boltz Dist.) and an opaque channel.

# Chapter 3

# Design of Multi-species Atomic Source

## 3.1 Previous Experimental Setup

Our existing experimental setup has been in operation, with various modifications, for the past six years and has performed well. A detailed performance of the system can be found in [16, 17]. The system excelled in its simplicity as it did not require a Zeeman slower or a $2D$ MOT to load the $3D$ MOT. The lithium MOT is loaded directly from an effusive source placed inside the quartz cell while the rubidium MOT was loaded by a dispenser. However, with future goals of dual species experiments it was unclear if such a system would produce sufficiently large samples of ultracold atoms from which to form molecules. When working primarily with lithium, the long MOT lifetime allowed for relatively large atomic samples (approximately $10^8$ atoms) despite modest loading rates. The downside of such a system is the wait time for loading the MOT decreases the repetition rate of the experiment which slows data acquisition. Unfortunately, when adding rubidium to the system the background pressure increases which in turn decreases the lithium lifetime leading to a smaller MOT. To load a rubidium MOT of approximately $10^8$ atoms results in lithium lifetimes on the order of seconds which would not suffice. This shorter lifetime could be mediated by decreasing the background pressure of rubidium, but this in turn results in a much smaller rubidium MOT. For example, reducing the rubidium background pressure to a level which only decreased the lithium lifetime by factor of two resulted in rubidium MOTS which contained on the order of $10^6$ atoms. This motivated the addition of the Zeeman slower as it isolates the sources from the science section while allowing for larger loading rates.

## 3.2 Simulation of Zeeman Slower Flux

Before constructing a Zeeman slower, a virtual slower was created to investigate the effect of various design parameters on the flux of cold atoms. The virtual slower was implemented in MATLAB and uses basic kinematic theory to determine the flux of cold atoms which can captured by the MOT.

The effusive oven and Zeeman slower produce a focused beam of cold atoms which can be captured by the MOT. Assuming the angular and velocity distribution of atoms leaving the effusive atomic source is known, the flux of cold atoms which

pass the through the MOT with a velocity less than the MOT capture velocity can be determined from geometry and simple kinematics. The Zeeman slower only affects the axial component of an atom's velocity and leaves the radial component unaffected. As a result, the trajectory of the atom will be parabolic and diverge away from the trap which leads to diminishing improvements as the slower is elongated. As a result of this divergence, only a fraction of the atoms which leave the oven at an angle less than some critical value reach the trap. This critical angle, ($\theta_{max}$), can be determined as follows. Assuming the oven orifice is focused at the MOT, an atom will miss the trap if the radial displacement during the time it takes the atom to reach the trap is greater than the MOT radius. The time needed to reach the trap can be divided into four parts: the time needed to reach the slower ($t_b$), the time in the slower before the atom reaches the necessary magnetic field to bring it into resonance with the slowing beam ($t_{off}$), the time during which the atoms are slowed to the exit velocity ($t_{on}$) and finally the time needed to reach the MOT after leaving the slower $t_a$. An atom, moving with velocity $v_{z,i}$, enters resonance with the slower beam a distance $z$ down the length of the slower which is given by:

$$z = \frac{v_{z,i}^2 - v_{z,f}^2}{2a} \tag{3.1}$$

The time of flight for the various stages can be calculated as follows:

$$\begin{aligned} t_b &= \frac{l_b}{v_{z,i}} \\ t_{off} &= \frac{l_z}{v_{z,i}} - \frac{v_{z,i}^2 - v_{z,f}^2}{2a v_{z,i}} \\ t_{on} &= \frac{v_{z,i} - v_{z,f}}{a} \\ t_a &= \frac{l_a}{v_{z,f}} \end{aligned} \tag{3.2}$$

where $v_z$ is the axial velocity given by $v\cos\theta$ and $v_r$ is the radial velocity given by $v\sin\theta$. The value $l_b$, $l_z$ and $l_a$ are the length atoms travel before, in and after the Zeeman slower, respectively and $v_{z,f}$ is the final axial velocity upon leaving the slower. The above expressions assumes that $v_{z,i}$ is greater than $v_{z,f}$. If that is not the

case, then the Zeeman slower has no effect and the time of flight is simply the total distance to the trap divided by the axial speed. Using these values, the maximum angle, $\theta_{max}$ can be determined using the following equation given a MOT radius, $r_{MOT}$.

$$\theta_{max} = \arcsin\left[\frac{r_{MOT}}{v(t_b + t_{off} + t_{on} + t_a)}\right] \tag{3.3}$$

For typical designs, the distance from the oven to the slower is much larger than the MOT radius and solving the above equation is greatly simplified by evoking the small angle approximation. This maximum angle depends on the initial velocity of the atoms. Now that the critical angle is determined, the angular and velocity distribution for an effusive source operating in the transparent regime derived in Section 2.2 can be used to calculate the total number of atoms entering the MOT which have been slowed below the MOT capture velocity, denoted as $N_c$, is:

$$N_c = \frac{W n \bar{v} A N_t}{4\pi} \int_0^{v_c} F(v)dv \int_0^{\theta_{max}} \kappa f(\theta) d\theta \int_0^{2\pi} d\phi$$

$W$ : Clausing Factor (see Equation 2.33)

$n$ : Density Inside Source

$\bar{v}$ : Average Velocity

$A$ : Orifice Area

$N_t$ : Number of Microtubes

$v_c$ : Capture Velocity of the Slower

$F(v)$ : Velocity Distribution (see Equation 2.31)

$\kappa f(\theta)$ : Angular Distribution of Emitted Atoms (see Equation 2.36) (3.4)

If the source is operating in the opaque regime, $\kappa$ and the velocity distribution must be modified in accordance with Equation 2.41 and Equation 2.48, respectively. For the design of the slower, the effect of the slower length on $N_c$ was investigated. Figure 3.2 shows the flux of capturable atoms as a function of slower length. Once the length is comparable to the distance the end is placed away from the MOT, the benefit of increasing the slower length is suppressed. For example

increasing the length of the slower from 20 cm to 30 cm only leads to increase in flux by 50%, while lengthening it from 10 cm to 20 cm leads to increase in flux by 200%.

This model neglects transverse heating due to the scattering of the slowing laser which results in the blooming of the atomic beam. This process can be thought of as a random walk resulting from the atoms uniformly remitting the absorbed photons from the slowing beam in all directions [25]. The root-mean-square displacement of the atoms at the end of a slower of length $L$ due to this process is given by:

$$< x^2 >= \sqrt{\frac{4v_{rec}}{9v_i}}L \tag{3.5}$$

where $v_{rec}$ is the recoil velocity due to the emission of a single photon and is given by $\hbar k/m$ [26]. For a one meter long slower, this effect amounts to an expected displacement of less than a millimetre for both lithium and rubidium which justifies this effect being neglected.

## 3.3 Design of a Zeeman Slower

### 3.3.1 Review of Existing Designs

Before building a Zeeman slower, a review of existing designs was conducted. The two key traits which differentiate the various designs is the mechanism which generates the field, in particular whether it is current driven or uses permanent magnets, and if the field is static or can be dynamically changed to optimize loading. It is difficult to directly compare the performance of Zeeman slowers as the flux of cold atoms is equally dependent on the atomic source which is coupled into the slower.

**Continuous Wire Wound**

Continuous wire wound slowers are the most commonly used design [25–27]. They consist of a single continuously wound solenoid where the number of windings is varied spatially to produce the desired field profile. The design benefits from the fact that only a single power supply is needed to power the slower. The downside of such a design is that it allows for no adjustment of the field once wound,

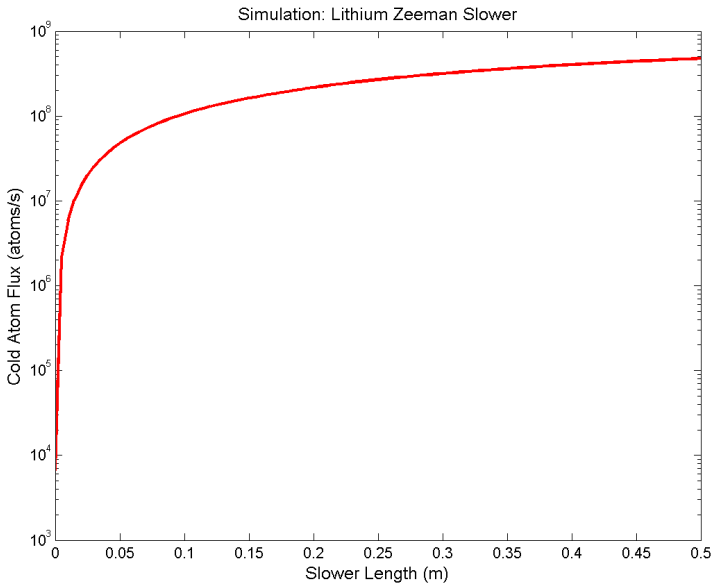


**Figure 3.1:** Simulation of capturable flux of lithium entering MOT located 20 cm from a slower of variable length operating with an $\eta = .6$ and final velocity of $20m/s$. The atoms are emitted from a source placed 60 cm from the slower with 90 microtubes of length 1 cm and inner diameter 200 $\mu m$. The source temperature is 400°C.

besides from increasing or decreasing the current. Furthermore, if the wire coating is damaged leading to a short circuit it could require extensive rewinding.

### Helical Wound Zeeman Slower

Unlike the continuous wire wound design, the helical wire wound Zeeman slower is made from single winding with varied pitch to produce the desired field pattern [28]. The design is easier to assemble as it does not require many hours of winding coils. However, to compensate for fewer windings much larger currents are needed which can be challenging to work with. Similar to the continuously wire wound slower, this design does not allow for modifying the slowing field aside from changing the current.

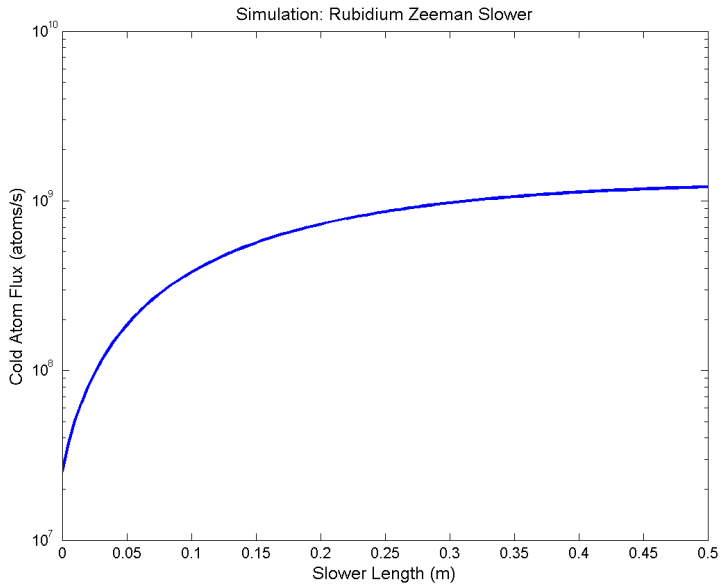


**Figure 3.2:** Simulation of capturable flux of rubidium entering MOT located 20 cm from a slower of variable length operating with an $\eta = .6$ and final velocity of $20m/s$. The atoms are emitted from a source placed 60 cm from the slower with 90 microtubes of length 1 cm and inner diameter 200 $\mu m$. The source temperature is 80°C.

### Segmented Slower

This design consists of separate solenoids with each current being independently controlled [29]. This allows for the field profile to be controlled remotely and changed in real time to optimize MOT loading rate. Furthermore, alternate designs such as $\sigma+$, $\sigma-$, and spin-flip magnetic fields to be easily tested. If a coil is damaged it does require that the entire slower be rewound. The downside of this design is the field will have small modulations in the magnetic field profile. It also requires a more complex current source.

### Transverse Field Slower

Another design approach is to run high current parallel to the slowing axis to produce the magnetic field transverse to the slowing beam. Such a design was

reported for the slowing of $^{85}$Rb and used two metal bars which carried the current [30]. The bars were machined with a specific profile such that they produced the desired magnetic field. Similar to the helical design, large current in excess of $100A$ was needed to produce the field. Another drawback is the slowing beam cannot have a well defined circular polarization as it does not propagate along the quantization excess set by the magnetic field. This design is appealing as it is simple to construct and can be easily removed or modified.

**Permanent Magnet Design**

Several designs have emerged which use permanent magnets. Such designs have the benefit of requiring no power supply or cooling. A permanent magnet based on the Halbach configuration has successfully loaded a MOT of $^{87}Rb$ and has the added benefit of being assembled after baking. Unfortunately, such a design would not work for two species slowers as the field cannot be changed.

To address the ability to modify the field, an alternative approach places the permanent magnets on stepper motors which vary the distance of the magnets from the slowing tube. This allows the fields to be optimized in real time to maximize slowing. However, to switch between species would take much longer than a current based approach.

### 3.3.2 Construction of Zeeman Slower

After reviewing existing design we decided to use a wire wound design consisting of eight separately wrapped sections. The rationale for such a design is it allows for modification of the slowing field quickly which is needed to switch between atomic species. Furthermore, the ability to independently control each coil allows for real time optimizing of flux. The slower length of 30 cm was decided upon based on the simulations in Section 2.1 which indicated that longer slowers did not yield significant improvements in flux. Secondly, a longer slower would require larger fields leading to increased heating which would require water cooling.

The slower consists of a 17 mm diameter tube divided into eight sections by metal plates. The plates are secured by aluminum rings which are wedged between the tube and plate. The tube diameter was chosen for three reasons: (1)

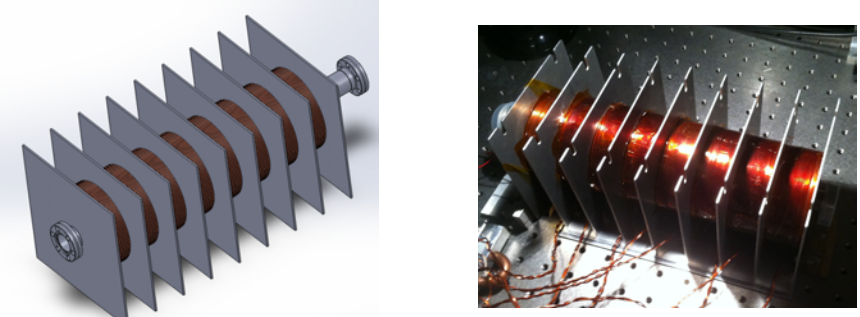

**(a)** SolidWorks Rendering

**(b)** Finished Zeeman Slower

**Figure 3.3:** SolidWorks rendering of the Zeeman slower along with actual slower.

the small inner diameter improves differential pumping, (2) the smaller radius of the solenoid leads to larger magnetic fields for a fixed current, and (3) it is compatible with CF-133 flanges. The coils consist of 20 axial windings and 25 radial windings of $16AWG$ insulating amide-amide polymeric magnetic[1]. The number of windings was selected such that the maximum voltage drop over the coil producing the largest field was $10V$ and the current required to produce fields did not exceed that specified for the wire gauge. For this slower, the optimal wire gauge was AWG16. After winding the coils, CF-133 flanges were welded to the tube. The complete design is shown in Figure 3.3.

### Magnetic Field from Segmented Slower

The magnetic field from a loop of wire with radius $R$ carrying current $I$ lying in in the x-y plane at a height h and distance $\rho$ away from z-axis is given by[31]:

$$B_z = \frac{\mu I}{2\pi}\frac{1}{(R+\rho)^2+h^2)^{1/2}} \times [K(k^2)+\frac{R^2-\rho^2-h^2}{(R-\rho)^2+h^2}E(k^2)] \tag{3.6}$$

$$B_\rho = \frac{\mu I}{2\pi\rho}\frac{h}{(R+\rho)^2+h^2)^{1/2}} \times [-K(k^2)+\frac{R^2+\rho^2+h^2}{(R-\rho)^2+h^2}E(k^2)] \tag{3.7}$$

[1] Manufactured by Superior Essex

where $K$ and $E$ are the complete elliptical integrals with argument $k^2$ equal to:

$$k^2 = \frac{4R\rho}{(R^2+\rho^2)^2+h^2} \tag{3.8}$$

In order to calculate the field from a single solenoid, the contribution from every coil loop, each having a slightly different radius and position, must be considered. Once the field for a single solenoid is known, the field for the entire slower can be calculated by convolving the single solenoid field profile with a train of eight delta functions separated by the coil spacing scaled by the appropriate current. Finding the currents which minimize the difference between the actual field and the ideal field is made easy by the fact the magnetic field is linear in current and therefore can be optimized using a linear least squares method. By defining a current vector, $\vec{I}$, whose elements are the initial guesses for currents in the solenoids, the current, $\vec{I}_{min}$, which minimizes the least squares difference between the fields is given by:

$$\vec{I}_{min} = \vec{I} - ([JJ^T]^{-1}J\vec{r})^T \tag{3.9}$$

$\vec{I}$ and $\vec{I_m}$ are both vectors of dimension $n$ equal to the number of solenoids. The residuals, given by $\vec{r}$, is a vector of dimension $m$ given by the difference between the ideal field and field produced by the current vector $I$ at position along the solenoid. The matrix $J$ is the Jacobian with dimensions $n \times m$ with element $J_{i,j}$ given by:

$$J_{ij} = \frac{\partial r_j}{\partial I_i} \tag{3.10}$$

The magnetic field produced by this design always exhibits slight modulations depending on the coil spacing and as a result will never perfectly match the desired field profile. However, as long as the gradient does not exceed the maximum value defined by Equation 2.19, the adiabatic slowing condition will be met. Figure 3.4 shows both the ideal field and the one returned from the least squares regression. The field gradient was also computed to ensure the adiabatic slowing condition was satisfied, this result is shown in Figure 3.5.

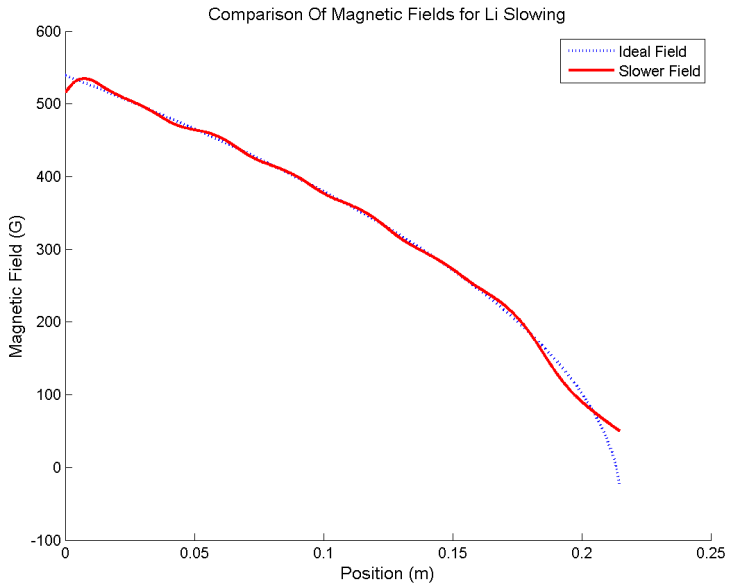


**Figure 3.4:** Comparison of the ideal slowing field and theoretical field produced by the segmented slower

### Matching Slower Field to the MOT Field

During the design of the Zeeman slower, the possibility of combining the Zeeman slower field and MOT field was investigated. This would have the benefit of raising the capture velocity of the slower by increasing its effective length and help mitigate the blooming of the beam by slowing closer to the trap. To verify the feasibility of this design two things had to be checked: (1) is it possible to smoothly connect the two fields and (2) would such a field be able to slow the atoms. To address the first question the same least squares algorithm was used, but this time the effect of the trapping field was included. The result of this fit is shown in Figure 3.6.

To verify the atoms could be slowed by such a design, a virtual slower was programmed which numerically solves the one dimensional equation of motion given the scattering force exerted by the slowing beam at a particular location. The program was run for different initial velocities and a phase space plot was calculated for the slower which is shown in Figure 3.7. The simulation parameters were: beam intensity of $s0 = 7$, a detuning $-80$Mhz, and $\eta = 0.5$. The virtual

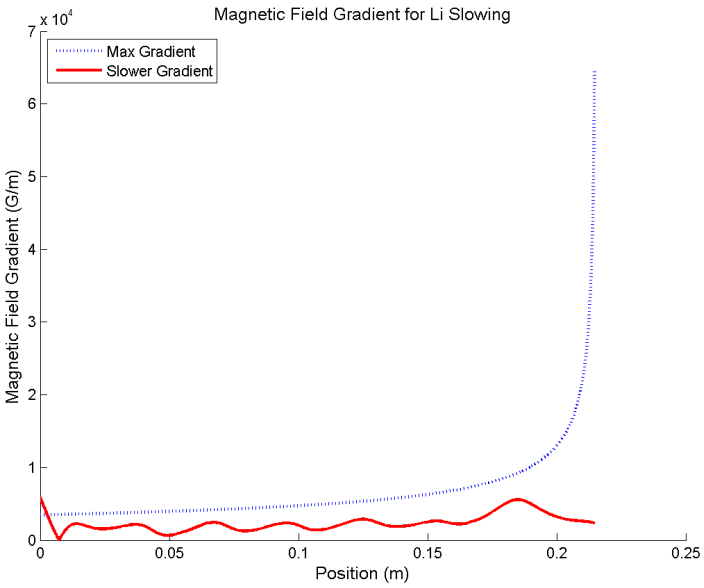


**Figure 3.5:** Comparison of the maximum allowable gradient as defined by Equation 2.19 and the theoretical gradients produced by the segmented slower

.

slower was able to slow atoms from 760 m/s to 30 m/s. The undulations in the magnetic field require a larger laser intensity than predicted by Equation 2.3 to ensure the adiabatic slowing condition is still met.

#### Verification of Magnetic Field

The magnetic field from the slower was measured using a hall sensor and was compared to the theoretically computed profile. Figure 3.8 shows a comparison of the theoretical slowing field to the field measured experimentally. The fields were compared for the entire slower and shown in Figure 3.9.

### 3.3.3 Computer Controlled Current Driver

One drawback of the slower design is that it requires multiple current sources to drive each solenoid. It is not feasible to purchase eight separate power supplies, in-

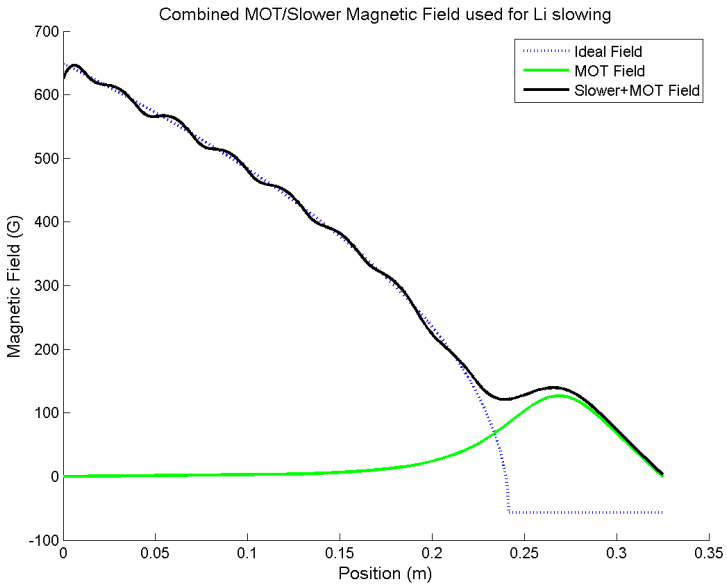


**Figure 3.6:** Magnetic field for the ideal case and hybrid case which combines both the MOT and slower field.

stead we elected to build a MOSFET controlled current source which can be powered from a single high current supply. In order to easily switch between atomic species and optimize load roads, the current source should have the ability to be controlled via computer. Therefore the current controller consists of two parts: the high power current board which distributes the current to slower and the computer control board which interfaces with our existing experimental control system.

### Current Distribution Board

The current distribution board consists of eight independent channels which drive specified currents based on a set point voltage. Each channel consists of a current sense resistor, a MOSFET, and gate-driver op-amp. Figure 3.10 is the circuit schematic for a single channel.

The circuit works by having the op-amp drive the difference between the set point voltage and voltage drop across the resistor to zero by controlling the current through the MOSFET. We chose to use the *OP*275 as it contains two devices per

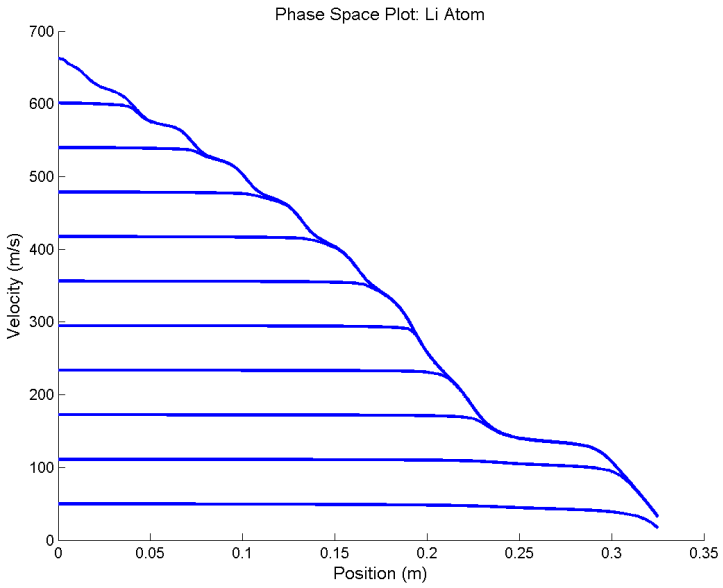


**Figure 3.7:** Phase space plot showing Li atoms being slowed by the field in Figure 3.6 by a laser with an intensity $s0 = 7$ and a detuning $-80$ Mhz.

package which allows for the second op-amp to be used as buffered monitor. It also has good low noise performance and can source considerable current which helps to quickly change the gate voltage. The combination of $R3$ and $C1$ form a low pass filter with a cut-off frequency of 100 kHz which limits the high-frequency gain and serves to stabilize the circuit. The current sense resistor is different for every channel as each solenoid is operated within a different range of currents. It is important to add a pin-wheel diode in parallel with the solenoid which clamps the back-emf when the current is switched off to protect the power supply and MOSFET. A small resister (50Ω) is placed in series with the MOSFET gate. This helps limit the effect of the large gate capacitance at the output of the op-amp which can lead to ringing and oscillations in the output. The current sense resistors should be chosen to have low sensitivity to changes in temperature as changes in resistance lead directly to systematic errors in current. Another important point is the PCB should be routed to ensure minimum return path resistance for the sense resistor to ensure the grounds for the reference voltage and sense resistor do not deviate

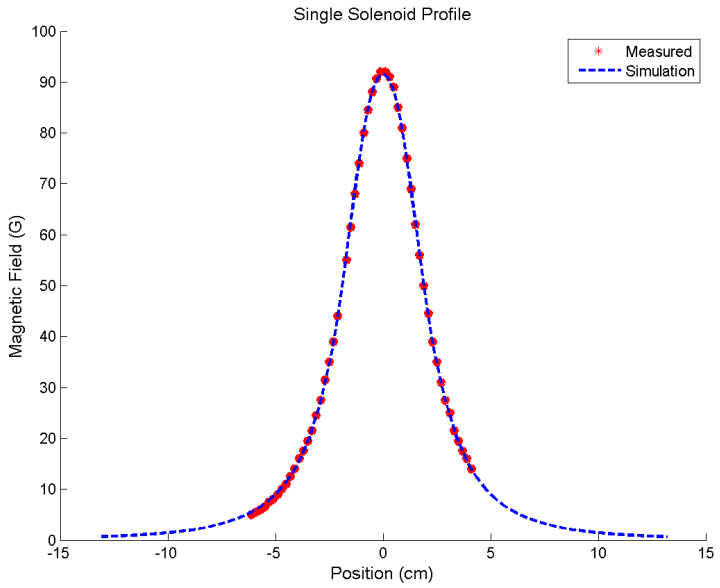


**Figure 3.8:** Magnetic field profile for a single solenoid.

significantly. Lastly, the MOSFET should be chosen to operate in saturation when being used as a current source as it will minimize the effect of power supply voltage fluctuations. However, this last point is challenging when designing a slower for multiple species which require different magnetic fields. The MOSFETs and sense resistors dissipate significant power, approximately 300 W in total, and the entire circuit must be water cooled.

### Computer Control Board

A common 50 pin utilities control bus (UT-BUS) is the communication backbone of our experiment. The bus consists of a 16-bit data bus, a 8-bit address bus, and a single strobe bit as shown in Figure 3.11. The strobe is clocked at 20 MHz and on every rising edge transition a new data word and address are written to the data bus and address bus. Devices which are controlled by the bus have a local address, typically set by a dip switch, which is compared to the bus address. If the two match, the data word is latched through.

For the Zeeman slower's computer control board, the 12 least significant bits

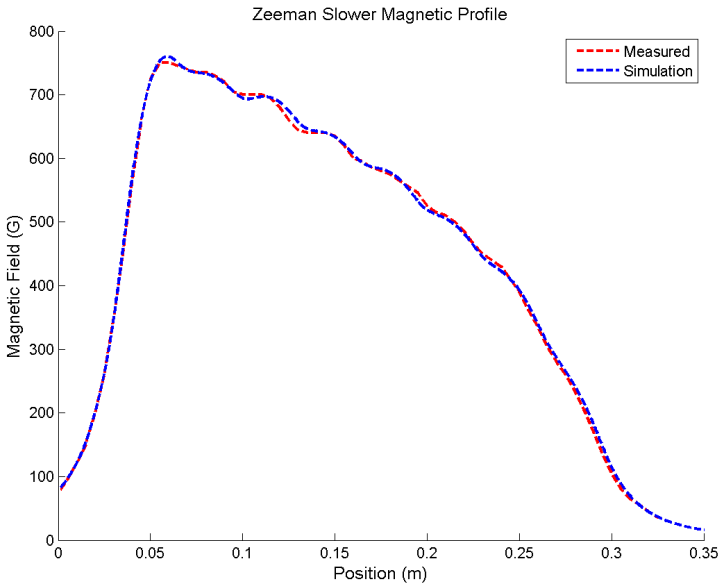


**Figure 3.9:** Magnetic field profile inside the Zeeman slower.

of the 16-bit data bus set the output voltage of a 12-bit Digital to Analog Converter (DAC) (model: AD5725 manufacturer: Analog Devices). Each board has two DACS, each of which has four output channels which drive the eight solenoids for the slower. The address bus selects a channel by first selecting the board (address bits 39-47), then one of the two DACS (address bit 37), then finally one of the four output channels is selected (address bits 33 and 35). The digital logic which selects a chip is shown in Figure 3.12. The strobe signal enters the comparator and passes through if the two addresses match. The AND and NOT gates following the comparator send the strobe bit to select one of the two DACS labeled as $CS1$ and $CS2$ in the schematic. The strobe bit is also delayed and is used to load the data into the memory register of the DAC and onto the analog output. The delay ensures the data has reached the DAC and is given time to stabilize.

The analog portion of the board consists of a $3.3V$ reference (model: ADR4533 manufacturer: Analog Devices) which provides a reference for the DACS. The voltage reference determines the highest voltage which can be sent to the current distribution board which in turn sets the maximum current. The board has a 6V

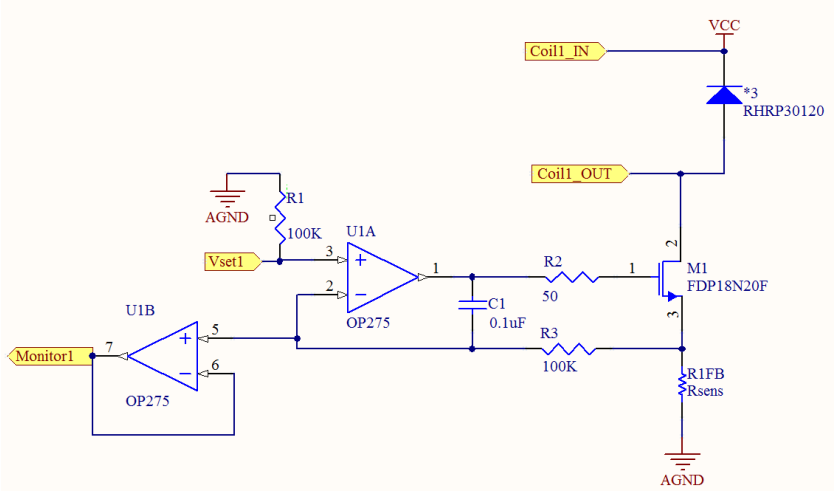


**Figure 3.10:** Single channel on the current distribution board, not shown is the bypassing capacitors on the op-amp (typical values used are 10$\mu$F tantalum cap in parallel with 100nF ceramic cap.

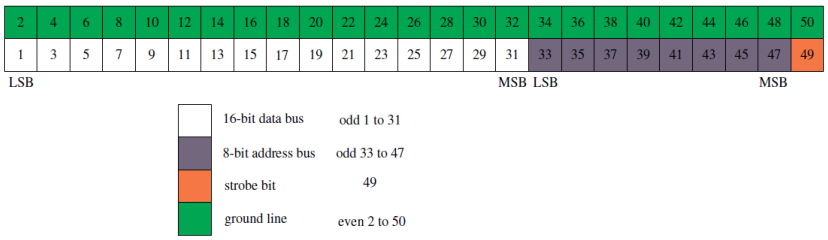


**Figure 3.11:** Pin out for UT control bus.

regulator which powers both DACS and voltage references. The board has a digital ground which is a reference for the digital logic circuitry and an analog ground for the DACS and 3.3V reference. The DACS also have a digital ground, but for noise performance it is best to connect that to the analog ground. The digital and analog ground should be connected at a single point via a ferrite bead and care should be taken to avoid ground loops.

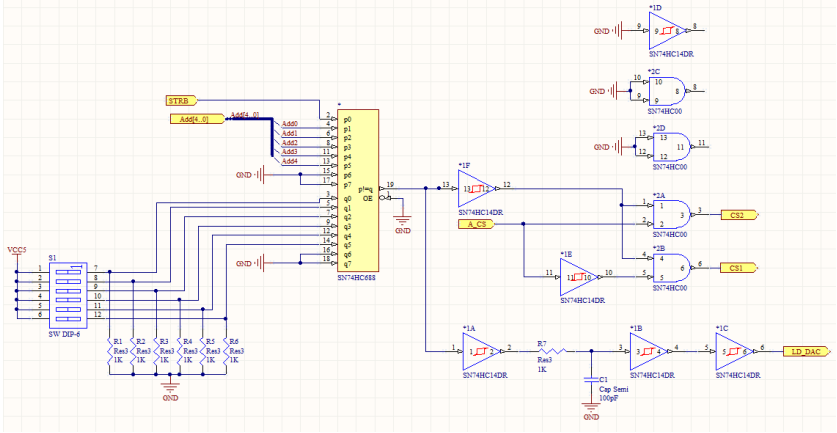


**Figure 3.12:** Digital logic circuitry used to select DAC.

## 3.4 Design of an Effusive Source

The effusive sources are the starting point for the experiment and care should be taken to ensure they operate as intended. They are required to produce well collimated atomic beams of approximately $10^{15}$ to $10^{16}$ atoms per second. In order to produce these fluxes, they are heated to achieve suitable vapor pressure within the source. As a result, the sources must be able to withstand high temperature; this is particularly true for lithium. As the lithium and rubidium atomic beams travel through the same Zeeman Slower, they must be emitted collinear. Finally, the vacuum system must baked at approximately $200°C$ in order to reach sufficiently low background pressures. At such temperatures, the rubidium reservoir would be quickly depleted. To prevent this, the rubidium is contained in ampule which is broken in situ after the bake-out. This section describes the design of the sources in order to meet these specifications.

The sources were built primarily from standard ConFlat Vacuum Flange (CF) vacuum parts. Figure 3.13 shows the two sources with lithium on the left and rubidium located underneath. The atomic beams exit the reservoirs through two offset openings. The openings are pressed fit with approximately 80 microtubes with $200\mu m$ ($300\mu m$) inner (outer) diameter.

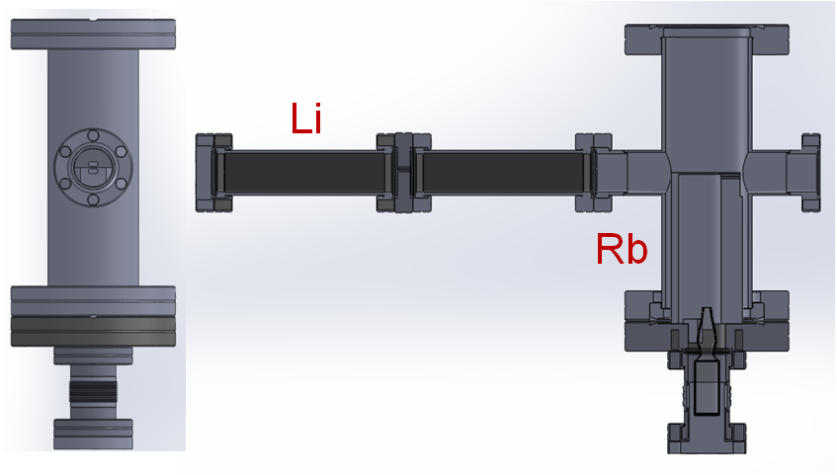


**Figure 3.13:** SolidWorks rendering of the two sources. Atoms leave the sources and travel towards the right into the science chamber.

### 3.4.1 Rubidium Source

The rubidium oven consists of an ampule holder, bellows, ampule breaker, and tower. The ampule's base is held in a cylindrical tube which is welded to a CF-133 blank and the top is held in a hole milled into the CF blank. The two blanks are attached via a flexible bellows which can be bent in order to break the ampule. To prevent the ampule from breaking prematurely, a pipe is slide over the two CF blanks to prevent the bellows from bending. Once broken, rubidium fills the bellows and tower where it then leaves via the microtubes. A removable backstop placed inside the oven, which can be seen in Figure 3.14, was machined to ease the insertion of the microtubes. The top of the tower is kept as thin as possible to minimize the space between the openings of the two sources. The source is heated by two band heaters, one of which heats the base of the rubidium tower to $100^{\circ}C$ and the other heats the pipe which keeps the bellows rigid to $80^{\circ}C$.

### 3.4.2 Lithium Source

The lithium source is much simpler than its rubidium counterpart as it is not required to break an ampule. The lithium is loaded directly into a CF-133 nipple which is sealed from the experiment with a CF blank. Similar to the rubidium

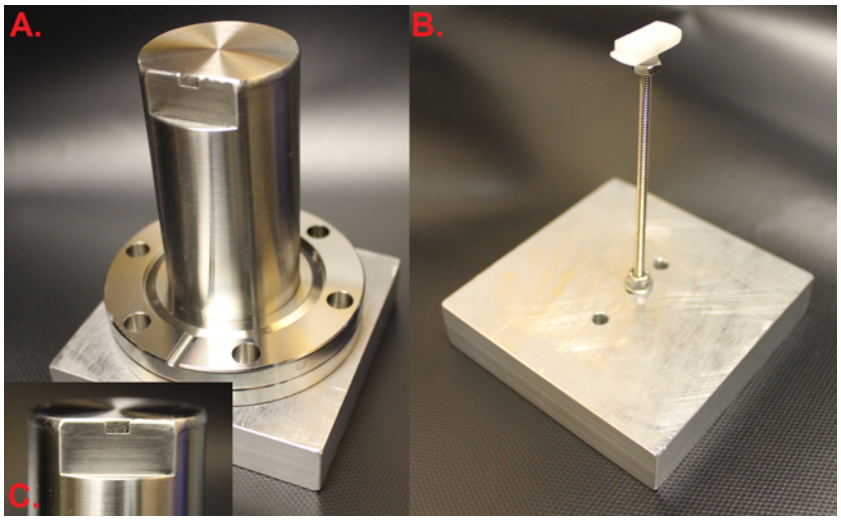


**Figure 3.14:** Rubidium effusive source is shown sub-figure A along with a close-up of the microtubes. The backstop is shown in sub-figure B.

source, a hole is milled into the blank in which microtubes are pressed fit. This can be seen in Figure 3.15 .

One important detail is that copper gaskets cannot be used for the lithium source. Lithium, especially when heated, is very corrosive and will quickly dissolve copper within a few hours. Figure 3.16 shows the end result of such process, the copper gasket was completely dissolved by the lithium and then condensed on the microtubes. Instead, annealed nickle gaskets should be used as they are not eroded by lithium. The oven is heated by two band heaters and wrapped in aluminum foil.

## 3.5 Design of Experimental Setup

### 3.5.1 Quadrupole Magnetic Field Coils

The ability to produce large magnetic fields and gradients is a prerequisite for atomic trapping and cooling. A MOT requires a field zero with a linear gradient to confine atoms while evaporation cooling in a dipole trap requires the tuning of the scattering lengths by a applying homogenous magnetic fields. The former field

**Figure 3.15:** CF blank which holds the microtubes for the lithium oven.

can be produced by two loops offset by their radius carrying equal currents in opposite directions, typically refereed to as the Anti-Helmholtz Configuration (AHC). The latter homogenous field is created with the identical coil configuration but with currents flowing in the same direction. This configuration is referred to as the Helmholtz Configuration (HC). Such configurations have the desired properties that the gradient is linear to $3^{rd}$ order for AHC while the $2^{nd}$ order contribution to curvature cancels for the HC. Using equation Equation 3.6 and Equation 3.7, to leading order the axial ,$B_z$, and radial fields, $B_\rho$ for the HC are:

$$\begin{aligned} B_z &= \mu I \frac{8}{5\sqrt{5}R} + ... \\ B_{rho} &= 0 + ... \end{aligned} \tag{3.11}$$

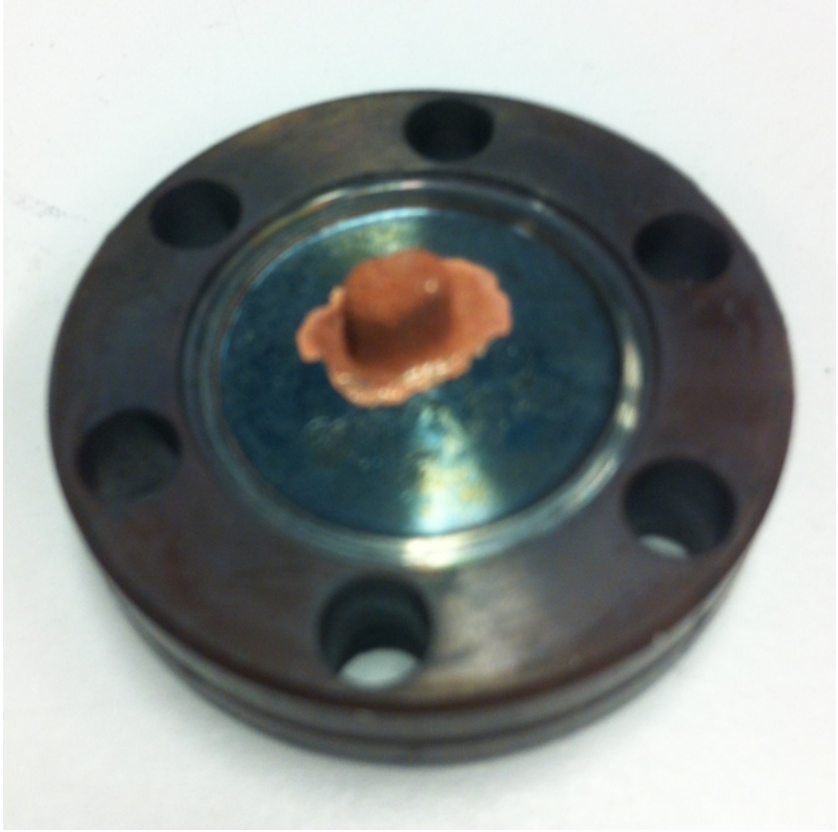

**Figure 3.16:** Copper covered microtube after the gasket was dissolved by the heated lithium.

while for the AHC the gradient is given by:

$$\begin{aligned} \frac{\partial B_z}{\partial z} &= \mu I \frac{48}{25\sqrt{5}R^2} \\ \frac{\partial B_\rho}{\partial \rho} &= -\frac{1}{2}\frac{\partial B_z}{\partial z} \end{aligned} \tag{3.12}$$

For our applications we desire homogenous magnetic fields in excess of 1kG. In order to maximize the magnetic field, the resistance of the coils should match the power supply's current and voltage limits. Our supply is a 100 V and 50 A linear supply and the coils are driven in series, hence each coil should have a resistance of 1Ω during maximum current operation. The rise in wire temperature should not

exceed $70°C$ which leads to a room temperature resistance of $0.85\Omega$. [2]. In order to fit in the existing coil mounts, the maximum outer diameter has to be less than 9 cm. The coils are enclosed in a housing which allows for water cooling and wound with Teflon spacers between every two windings to ensure all wires have direct contact with the water. The quartz optical cell limits the minimum spacing between the coils to 4.5 cm which defines the coil radius for the Helmholtz configuration. However, in this ideal Helmholtz configuration the existing power supply would not allow us to reach the desired fields. Therefore, the inner radius needs to be decreased at the expense of field homogeneity. The inner radius is also limited by the $2''$ vertical imaging optics to a minimum value of 30 cm. A computer program was written which iterated through possible wire gauges and filled the available space inside the coil house with windings. It calculated the magnetic field and the homogeneity in the HC along with the gradient for the AHC. Finally, it returned the expected resistance of the coil given the length of wire needed for winding. The best resistance match was $14AWG$ with 23 radial windings and 11 axial windings. The properties of such a coil is listed in Table 3.1:

**Table 3.1:** Simulated magnetic field properties of the MOT coils.

| Parameter | Value |
|---|---|
| Maximum Field per Amp in HC | 32 G/A |
| Maximum Gradient per Amp in AHC | 3.8 G/A · cm |
| Homogeneity in HC over $1mm \times 1mm$ region | 60 ppm |
| Resistance | $0.88\,\Omega$ |

Below are contour plots showing the magnetic fields for both the Helmholtz and anti-Helmholtz configurations.

### Design of Coils

The final coil design consists of three parts: a lid, a base, and a retaining ring. All three parts are made from Delrin. Barriers are machined into the inside of the lid and base to force water through the windings. The retaining ring has two semi-circle sections which bolt together to secure the inner wall and prevent the coils

[2] The resistance of copper is given by $R = R_0(1 + \alpha(T - T_0))$ where $\alpha$ is $3.9 \times 10^{-3}\,°C^{-1}$

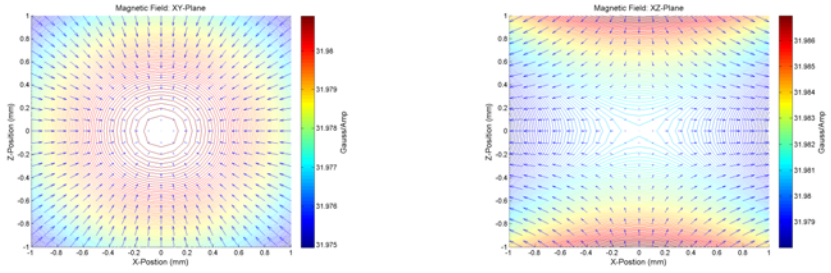


**(a)** XY-plane **(b)** XZ-plane

**Figure 3.17:** Magnetic field produced by the Helmholtz configuration. The field exhibits a saddle point in the middle of the two coils.

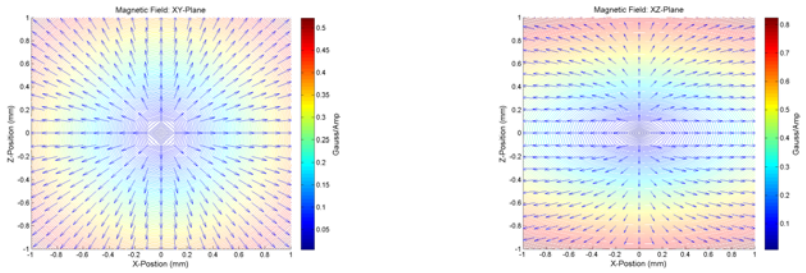


**(a)** XY-plane **(b)** XZ-plane

**Figure 3.18:** Magnetic field produced by the anti-Helmholtz configuration. The gradient is twice as large in the z direction due to $\nabla B = 0$.

from bulging when under water pressure. Two O-rings, one between the lid and outer wall and the other between the base and inner wall, maintain a water tight seal. The coil housing was stress tested to 80 psi and did not leak. Figure 3.19 shows a SolidWorks rendering of the coil.

### Thermal Testing of MOT Coils

The coils were tested with flow rates from 2.8 L/min to 8.6 L/min while monitoring the average wire temperature for currents ranging from 5 to 50 A. At the maximum tested flow rate of 8.6 L/min and 50 A, the average wire temperature was 41 °C. At this flow rate, the thermal resistance is 5.5°C/kW. Figure 3.20 is a series of plots showing the coil heating as a function of flow rate, $\dot{Q}$.

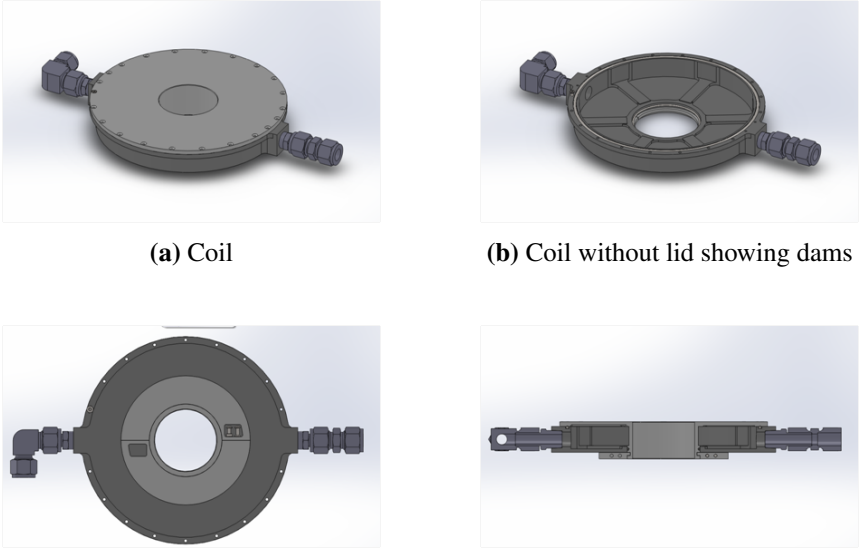

**(a)** Coil

**(b)** Coil without lid showing dams

**(c)** Bottom showing retaining ring

**(d)** Cross section showing O-ring groves

**Figure 3.19:** SolidWorks rendering of the MOT coils.

From these heating curves, the thermal resistance of the coils as a function of flow rate can be extracted. Note, the thermal resistance is the slope of the line which relates the rise in average wire temperature and power dissipation as follows ($\Delta T = R_{th}P$). To first order, the thermal resistance scales linearly with the inverse flow rate as:

$$R_{\text{th}} = R_{\text{th,WireToWater}} + \frac{m}{\dot{Q}} \tag{3.13}$$

The first term describes the thermal resistance between the wire and water. Physically, it is the thermal resistance as the flow rate goes to infinity and measures the ability to transfer heat from the wire to the water through the insulating coating. This number is of great interest as it determines the rate limiting step in heat flow out of the coils. The slope of the line, $m$, accounts for how an increase in average water temperature leads to an increase in average wire temperature. By extracting slopes from data in Figure 3.20, the thermal resistance from each flow rate can be determined. This result is shown in Figure 3.21.

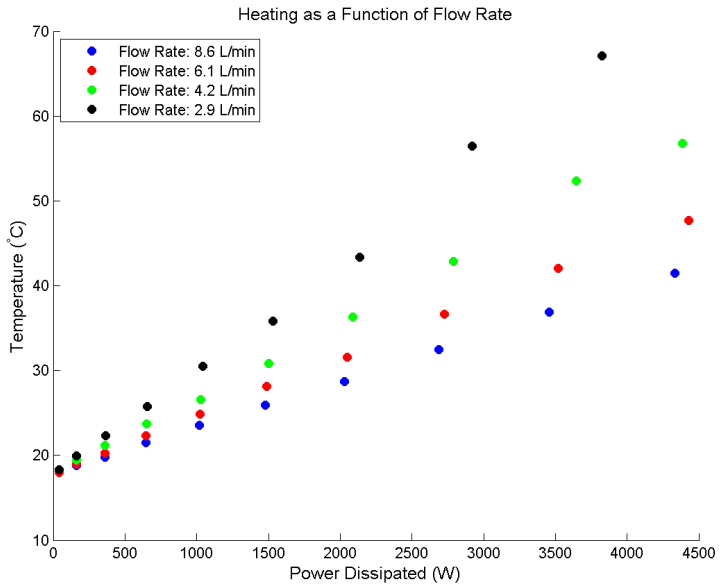


**Figure 3.20:** Coil heating as a function of current for various flow rates. The slope of the line gives the thermal resistance.

The thermal resistance of the wire to water interface is 2.3 °C/kW. This is in reasonably good agreement with the theoretical resistance expected for the insulating coating of 1.5 °C/kW, in addition to any thermal contact resistance at the water to coating and coating to copper interfaces.

### Magnetic Field Testing of MOT Coils

Once completed, the MOT coils were tested to ensure the fields matched the theoretical profile. Due to spatial constraints the final coil housing was only able to accommodate 21 radial windings and 10 axial windings. Figure 3.22 and Figure 3.23 show the measured field profiles compared to the theoretical profile for the Helmholtz and anti-Helmholtz configurations. A summary of the measured fields for both MOT and compensation coils can be found in Table 3.2.

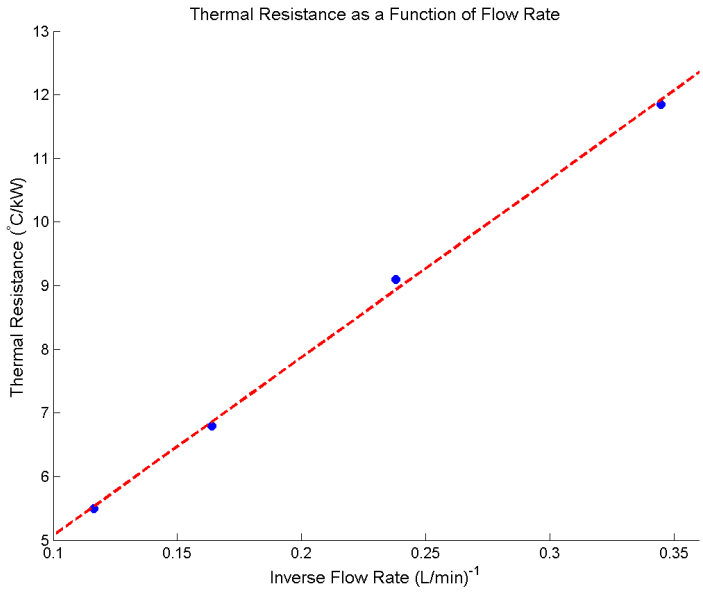


**Figure 3.21:** The thermal resistance of the coil as a function of flow rate. Each point is from the slope of a curve in Figure 3.20.

### 3.5.2 Verification of Magnetic Fields from Compensation Coils

The MOT requires three sets of compensation coils, one for each axis, to provide offset fields to move the location of the zero field position. They are also used to move the MOT when compressing it and loading into dipole traps. We plan to also use the z-axis compensation coils to provide a gradient to compensate for gravity and/or residual gradients resulting from the atoms not being well centered between the coils. The required gradient to compensate a force $F$ is given by:

$$\frac{dB}{dz} = \frac{F}{\mu h} \tag{3.14}$$

where $\mu$ is the magnetic moment (in units of frequency) and $h$ is Planck's constant. For lithium, the required gradient to compensate for gravity is 1 G/cm. The z-axis coils are integrated into the MOT coil housing which helps with cooling. Figure 3.24 and Figure 3.25 show the measured field profile compared to theoretical profile for the Helmholtz and anti-Helmholtz configurations.

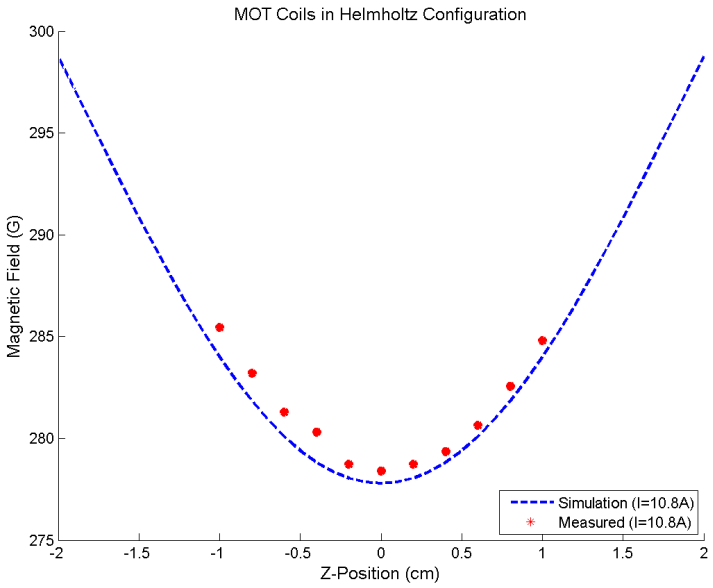


**Figure 3.22:** Magnetic field produced by the MOT coils with current of I = 10.8A for the HC (red dots) along with the simulation (blue line).

The y-axis coils produce fields perpendicular to the cell while the x-axis coils produce fields parallel to the cell. The properties of all the compensation coils and MOT coils are outlined in the Table 3.2.

**Table 3.2:** Magnetic fields per amp produced by the various coils in the experimental setup. Gradients for x and y coils are not measured as they are run exclusively in HC.

| Coil | Field at Center in HC (G/A) | Axial Gradient in AHC (G/(A·cm) |
|---|---|---|
| MOT Coils | 25.8 | 6.15 |
| Z-Compensation | 13.9 | 3.6 |
| Y-Compensation | 2.67 | – |
| X-Compensation | 1.45 | – |

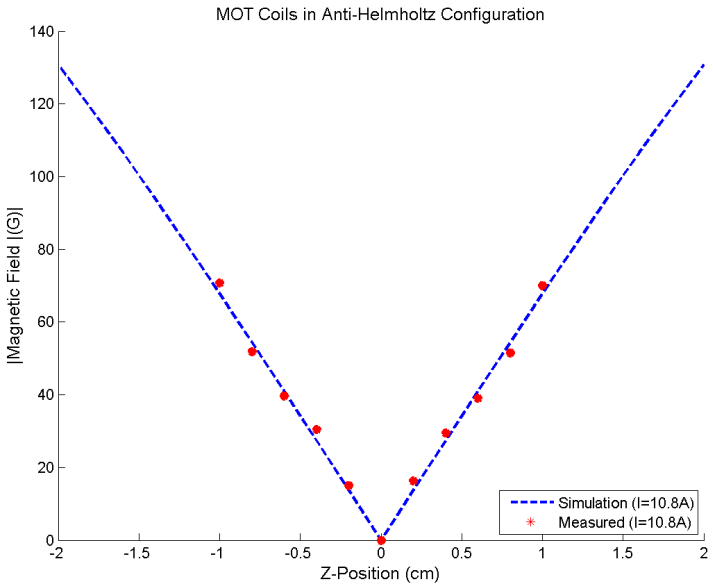


**Figure 3.23:** Magnetic field produced by the MOT coils with a current of I = 10.8A for the AHC (red dots) along with the simulation (blue line).

#### Maximum Homogenous Magnetic Field

The maximum homogenous magnetic field capable of being produced by the MOT coils is 1300 G and is limited by the maximum current of the power supply of 50 A. Neglecting the limitation of the power supply, the maximum achievable field when constrained by keeping the average wire temperature below 70°C at a flow rate of 8.5 L/s is 2100 G. This corresponds to a current of 80 A.

### 3.5.3 Vacuum System

The experimental apparatus consists of two sections: a source side which has the Rb and Li effusive sources and a science side which contains the quartz cell in which we perform experiments. The two sections are both pumped with an ion pump (model: VacIon Plus 20 Starcell manufacture: Varian) and a Non-evaporable getter (NEG) (model: CapaciTorr D 400-2 manufacturer: SAES). The two sections are connected by a differential pumping tube with inner diameter of 6 mm and

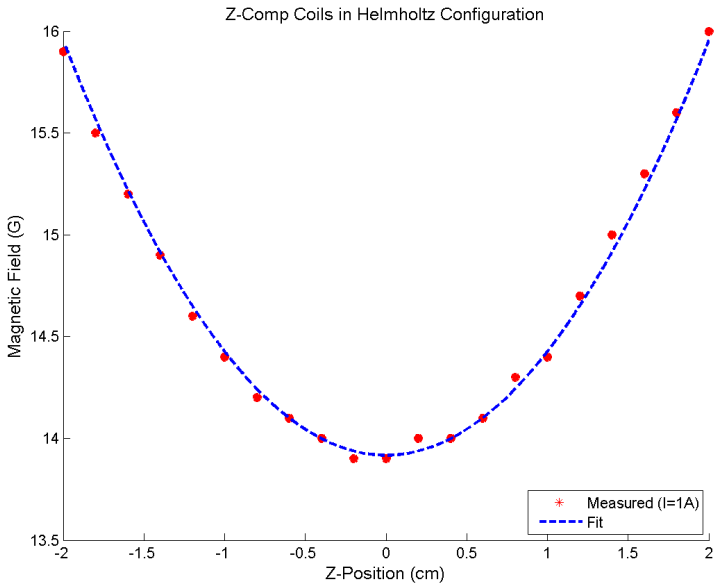


**Figure 3.24:** Magnetic field produced by the z-axis compensation coils with a current of 1 amp for the HC (red dots) along with a quadratic fit (blue line).

length of 12 cm. The differential pumping machined from a single stainless steel rod which is bolted to the CF reducer which connects the Zeeman slower to the six-way cross and can be seen is Figure 3.26.

The two sections are furthered isolated by a gate valve[3] which allows the sources to be replenished without exposing the science section to atmosphere. The gate valve is not all-metal valve and the air tight sealed is maintained with a Viton O-ring. Finally, there is a general purpose six way cross which allows for optical access to the atomic beams prior to entering the slower via two view ports. The cross also has a manual shutter and a copper feedthrough which can be used as a cold finger to reduce the background pressure of Rb. The mechanical shutter can also be used to reflect the Zeeman slowing beam out of the chamber which helps during alignment. Initial Residual Gas Analyzer (RGA) tests of the Li oven showed that when operational, the background pressure in the source side rose to low $10^{-8}$

[3]Manufacture: VAT Vacuum Valves Model: Series 010

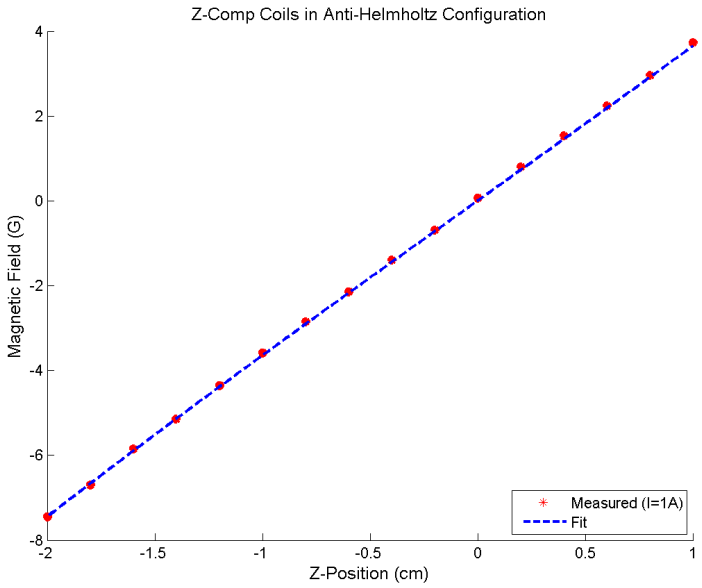


**Figure 3.25:** Magnetic field produced by the z-axis compensation coils with a current of 1 amp for the AHC (red dots) along with a linear fit (blue line).

torr range. The target pressure in the science section glass cell, PC, is below the $10^9$ torr range and must be maintained by the differential pumping. Figure 3.27 shows a cross section of the apparatus.

To estimate the conductance between the two sections, the NEG on the source side was heated in order to increase the background pressure of hydrogen to $10^{-5}$ torr. The pressure at the source side ion pump, $P_1$, and science side ion pump $P_2$ were estimated from the ion current. The pressure $P_1$, $P_2$, and $P_c$ are related by the conductance and the mass flow, $Q$, emitted from the heated getter via the following expression:

$$Q = (P_1 - P_c)C_1 = (P_c - P_2)C_2 = (P_1 - P_2)C \tag{3.15}$$

where $C_1$ is the conductance between the heated NEG and the cell and $C_2$ is the conductance between the cell and the ion pump on the science side. The total conductance, $C$, between the heated NEG and the science side ion pump is:

**Figure 3.26:** SolidWorks rendering of the differential pumping tube.

$$C^{-1} = C_1^{-1} + C_2^{-1} \tag{3.16}$$

In steady state, the hydrogen which passes through the differential pumping tube is pumped out of the system by the NEG and ion pump at a rate given by:

$$Q = P_2(\Gamma_{NEG} + \Gamma_{ionpump}) \tag{3.17}$$

where $\Gamma$ is the pumping speed of the pump. Combining Equation 3.15 and Equation 3.17 leads to relation between $P_1$ and $P_2$, under the assumption of $P_1 \gg P_2$, given by:

$$\frac{P_2}{P_1} = \frac{C}{\Gamma_{NEG} + \Gamma_{ionpump}} \tag{3.18}$$

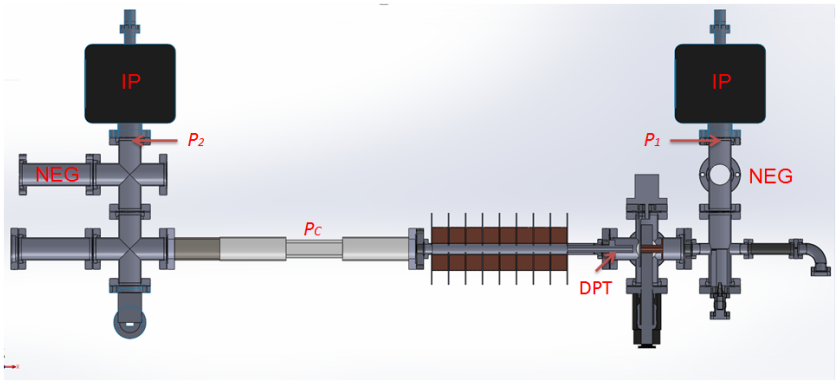


**Figure 3.27:** Cross section of the experiment. The ion pumps (IP) are labeled and used to estimate the pressures $P_1$ and $P_2$. The two sections are separated by a differential pumping tube labeled as DPT (6mm dia. 12mm length).

The relation between the cell pressure and source pressure is now:

$$\frac{P_C}{P_1} = \frac{C_1 + \frac{P_2}{P_1}C_2}{C_1 + C_2} \approx = \frac{C_1}{C_2}(1 + \frac{C_2}{\Gamma_{NEG} + \Gamma_{ionpump}}) \tag{3.19}$$

The above approximation is valid for $C_2 \gg C_1$. The conductance of a circular tube of length $L$ in centimeters and diameter $D$ in centimeters for a gas with mean velocity $\bar{v}$ is:

$$C_{tube} = 2.6 \times 10^{-4} \bar{V} \frac{D^3}{L} \tag{3.20}$$

The dominant contributor to the background pressure is hydrogen for which the conductance at room temperature is:

$$C_{tube} = 47 \frac{D^3}{L} \tag{3.21}$$

Table 3.3 lists the conductance for the various parts of the vacuum system.

From Table 3.3, it is clear that $C_1$ can be reasonably approximated as simply the differential pumping tube while $C_2$, which consists of contributions from the two CF-275 crosses and half the quartz cell, is approximately 40 $L/s$. The pumping speeds for hydrogen for the NEG and ion pump are 100 $L/s$ and 15$L/s$ respectively.

**Table 3.3:** Conductance for hydrogen of the various vacuum components.

| Part | Length[cm] | Dia.[cm] | C [L/s] |
|---|---|---|---|
| Differential Pumping Tube | 12 | 0.6 | .85 |
| Zeeman Slower | 30 | 1.8 | 9 |
| Cf-275 Cross | 15 | 3.6 | 143 |
| Quartz Cell | 35 | 3 | 42 |

Hence, the pressure ratio between the outlet of NEG ($P_1$) and inlet of the science side ion pump ($P_2$) as defined in Equation 3.21 is 130. The pressure differential between the cell and source defined in Equation 3.19 is 0.03 which is a reduction is pressure by a factor of 30. This pressure ratio is hard to measure experimentally, but the ratio $P_1$ to $P_2$ can be inferred from the ion currents. Assuming the pressure inside the science section scales as:

$$P_2 = P_{2,0} + \frac{C}{\Gamma_{NEG} + \Gamma_{ionpump}} P_1 \tag{3.22}$$

where $P_{2,0}$ is the background pressure prior to heating up the NEG. In order to verify the differential pumping, the NEG was heated while the ion current from both pumps was measured at various hydrogen pressures. The result is shown in Figure 3.28 along with a fit to Equation 3.22. The fit returned the hydrogen conductance of the differential pumping tube of 1.1 L/s assuming a total pumping speed of 110 L/s. This is in reasonable agreement with the theoretical value of 0.85 L/s.

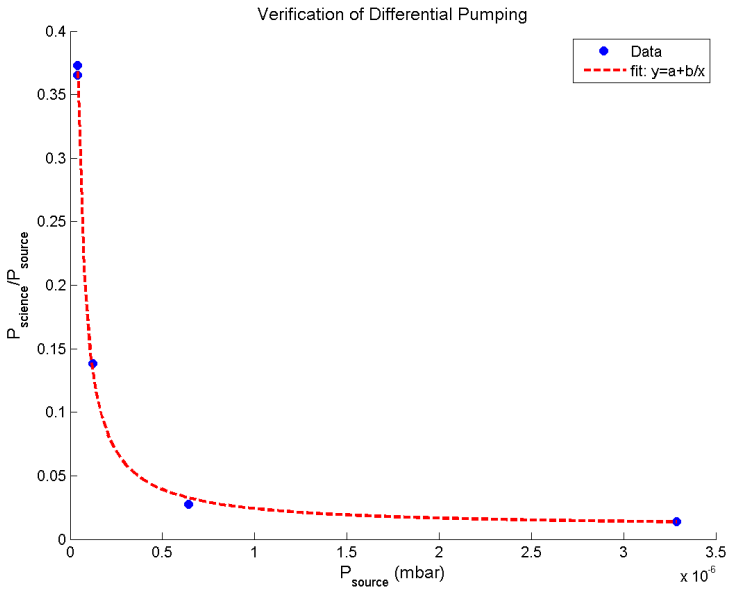


**Figure 3.28:** Pressure ratio between source and science section of experimental apparatus during NEG heating tests used to infer conductance of differential pumping tube.

# Chapter 4

# Characterization of Multi-species Atomic Source

## 4.1 Characterization of the Lithium Oven

Prior to installing the lithium oven into the experimental apparatus, it was important to verify that its operates as expected. In particular, we are interested in the atomic beam's flux, i.e. how many atoms are leaving the oven per second, angular distribution, and finally velocity distribution. Spectroscopic probing of the atomic beam is the most convenient method to measure these desired properties. From the resulting florescence signal one can infer the flux and transfer Doppler broadening. Unfortunately, it is challenging to simultaneously measure the angle and velocity distribution from the Doppler broadened spectrum as the two are inherently coupled.

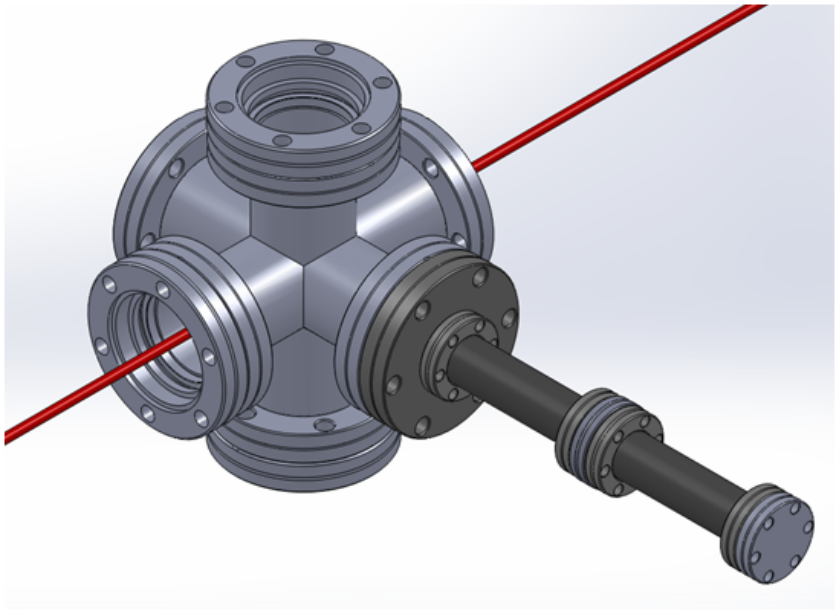

**Figure 4.1:** Experimental setup used to conduct the initial diagnostics tests of the atomic beam. The lithium oven is in the bottom right corner. Not shown is vacuum pump system.

Figure 4.1 shows the experimental setup for fluorescence imaging. The laser source for the diagnostic tests is from a home built external cavity diode laser [32]. The florescence signal was detected with a high sensitivity photodiode. The probe beam had a total of power of 0.4mW and a beam waist of 0.25mm. Figure 4.2

shows a picture taken of florescence emitted from the atomic beam when the laser is tuned to the D2 transition and scanned over the hyperfine ground state levels.

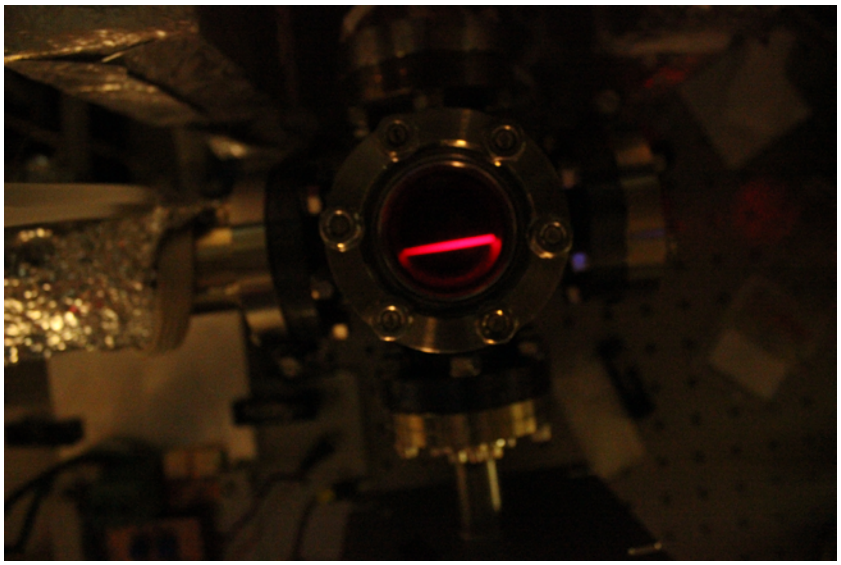

**Figure 4.2:** Florencense signal observed from the effusive source without the nichrome mesh lining. The lithium source is at the top and the atomic beam travels downwards while the probe beam goes from left to right.

It was immediately evident that the atomic beam was not well collimated and upon closer inspection it appeared that lithium had leaked out of the oven. This had been observed with previous oven designs and was mediated by lining the oven with a mesh made from nichrome. The hypothesis for why this helps to ensure the lithium remains in the oven is that the mesh provides a scaffolding to which the lithium preferential adheres to. This prevents lithium from leaking out or being drawn out of the oven through the microtubes. Figure 4.3 shows the florescence after installing nichrome mesh which shows the improved collimation.

The majority of atomic sources which utilize microtubes insist on keeping tubes much warmer (50°C hotter) than other parts of the source to prevent clogging [33]. However, we chose to operate the oven with microtubes at same temperature or slightly warmer (10°C hotter) than the back of the oven. The reasoning is that at the operational temperatures of the oven, lithium is in the liquid phase and thermal gradients will lead to a wicking force drawing the liquid toward the microtubes if

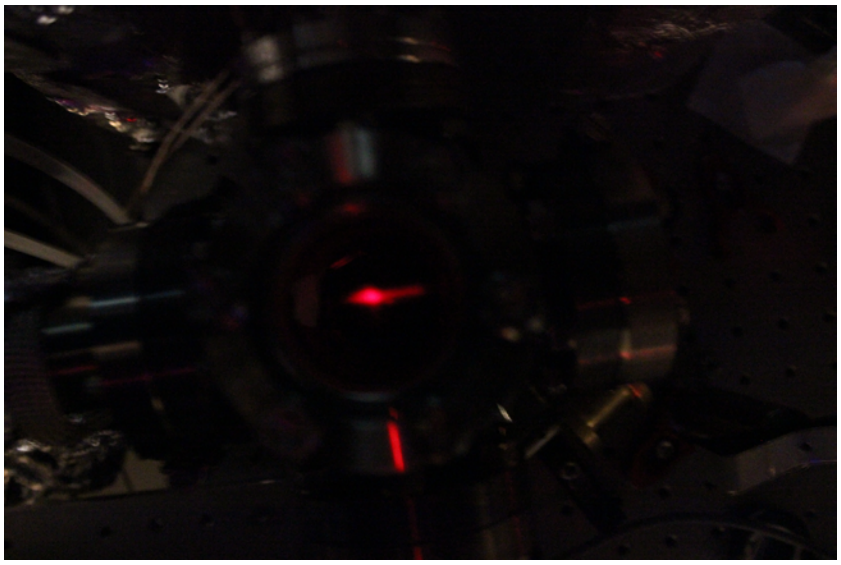

**Figure 4.3:** Florence signal observed from the oven due to the probe beam with the nichrome mesh lining.

they are the warmest. As this was previously observed to be an issue, the entire source is operated at the same temperature between $400-450$°C. The oven was operated for a week at this temperature while monitoring the florescence and no change in flux brightness or angular distribution was observed.

### 4.1.1 Measuring Angular and Velocity Distribution of the Atomic Beam with Florescence

It is difficult to determine the angular and velocity distribution with florescence alone as the Doppler broadening couples the two distribution via $k \cdot v$. Therefore, it is best to try to measure the two independently. In practice it is much easier to produce a beam with minimal angular distribution using apertures compared to trying to narrow the velocity spread. If the atomic beam is well collimated, then a laser beam angled to the atomic beam directly probes the longitudinal velocity distribution. To collimate the atomic beam, it is passed through the Zeeman slower which acts as an aperture. The probe laser is then split in two with one beam intersecting the beam at 90° and the other at 45°. The first beam can be used to

calibrate the laser's frequency based on the hyperfine splitting while second can be used to measure the Doppler shift. The described setup is depicted in Figure 4.4. The geometric constraints limit the maximum divergence angle of the atomic beam to approximately 1°.

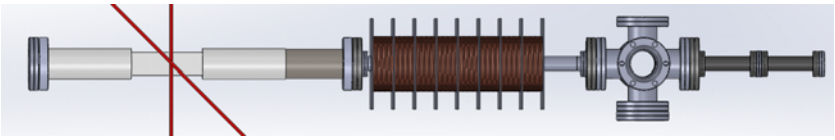

**Figure 4.4:** SolidWorks rendering of the apertures used to measure the thermal distribution of the atomic beam. The atomic beam goes from right to left.

The florescence signal, $F_{beam}$, emitted from an atomic beam with zero angular divergence from a laser beam bisecting at an angle $\theta$ with intensity $I$ much less than $I_{sat}$ and frequency $f$ is given by:

$$\mathrm{F}_{beam}(f, f_0, T, \gamma, \theta) = C \int_0^\infty f(v) L(f - f_0 - \frac{k \cdot v}{2\pi}, \gamma) dv \tag{4.1}$$

where the integral is over all velocities, $f(v, \alpha)$ is velocity distribution in an atomic beam given by Equation 2.31, and $L$ is the standard Lorentzian line shape centered at $f_0$. The temperature dependence enters through $\alpha$ in the velocity distribution.The parameter $C$ is a constant which depends on the intensity of light, scattering cross section, and density of atoms in the atomic beam. For extracting the velocity distribution this constant is irrelevant, but will be important for extracting the beam flux. The florescence signal observed contains four peaks resulting from the two probe beams exciting the 2 hyperfine levels in the ground state. The features produced by the perpendicular beam are easily resolvable, while those produced by the angled beam are not due to Doppler Broadening. The effusive source temperature was measured using a thermal couple to be $475°C$ and Figure 4.5 shows the observed florescence signal along fit using Equation 4.2. The model also includes a linear offset to account for unwanted background signal due to scattering of the probe beam. The frequency is changed by sweeping the diode current which also leads to a ramp in intensity. The model neglects this effect and assumes the intensity is constant as the change is on the order of a few percent.

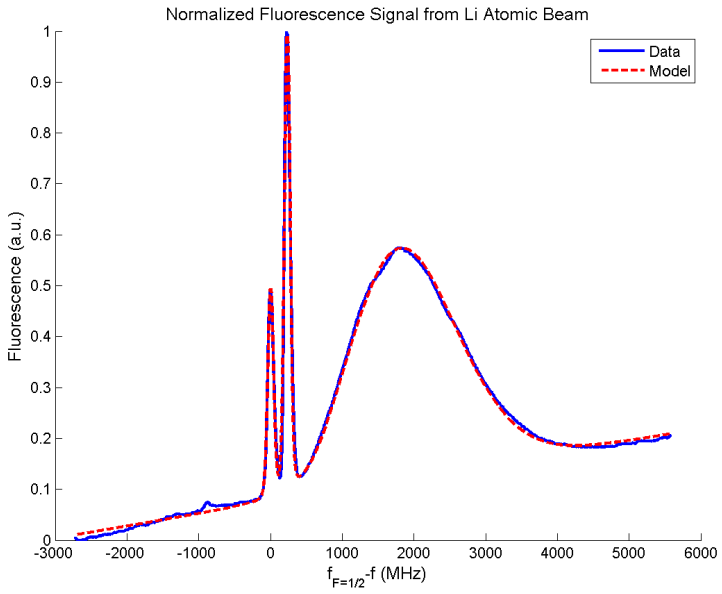


**Figure 4.5:** Fluorescence signal from the two probe beams used to measure the thermal distribution emitted from the atomic source.

$$\begin{aligned}\text{Signal}(f) =& C_1\text{Voight}(f, f_{F=1/2}, \gamma, T_{transverse})+ \\ & C_2\text{Voight}(f, f_{F=3/2}, \gamma, T_{transverse})+ \\ & C_3\text{F}_{beam}(f, f_{F=1/2}, T, \gamma, \theta)+ \\ & C_4\text{F}_{beam}(f, f_{F=3/2}, T, \gamma, \theta)+ \\ & \text{A}\times f + \text{B}\end{aligned} \tag{4.2}$$

The parameter $f_{F=1/2}$ and $f_{F=3/2}$ are the D2 resonance frequencies for the $F = 1/2$ and $F = 3/2$ ground state levels, respectively. The Voight profiles correspond to the signal produced by the transverse laser beam and the values returned by the fit for the two peak locations are used to confirm the frequency ramp of the laser. The temperature inside the atomic source can be extracted using the signal from the beam angled 45°. The resulting temperature from fit was $475°C$ which is in good agreement with the measured value.

Once the temperature of the beam was confirmed, the angular distribution and atom number can be inferred. The atomic beam is probed by a transverse beam immediately at the output of the oven as shown in Figure 4.1. The photodiode voltage signal is shown in Figure 4.6 along with the result of a numerical simulation of the expected florescence signal. The simulation varies the total flux from the oven and angular distribution to best fit the observed data. A more detailed description of the simulation can be found in Appendix C. The atomic source was operated at 450°C while the probe beam had a beam waist of approximately 2mm and total power of 450 $\mu$W. The total flux from the oven based on the simulation was $9.2 \times 10^{15}$ atoms/s with the FWHM of the angular distribution of 2.9°. The expected flux at this operational temperature is $2 \times 10^{15}$ atoms/s which is in very good agreement with the measured value. The FWHM is approximately 2.5 times broader than the expected angular distribution based on the microtube geometry. Possible explanation for the discrepancy are: (1) microtubes are not all collinear, (2) microtubes are not well packed which lead to large gaps between tubes which emit atoms, and/or (3) gaps between the tubes and the edge of the hole in the CF blank are emitting atoms. Regardless, the broader distribution will not significantly affect the performance of the slower and any decrease in center line intensity can be compensated for by increasing the oven temperature.

## 4.2 Characterization of Zeeman Slower

### 4.2.1 Characterization of the Slower with an Atomic Beam

The slower was initially tested using the experimental setup depicted in Figure 4.4 with a single probe beam angled at 45° to the atomic beam. The magnetic field and detuning were set to slow to a final velocity of 350m/s and the resulting velocity distribution is shown in Figure 4.7. The dip in the top of the peak was a result of the tapered amplifier which was used to generate the slowing beam being improperly seeded resulting in significant amplified spontaneous emission.

Although the slower was tuned to ensure the atoms leave with a final velocity of 350m/s, the resulting peak of slow atoms is centered at 240m/s. The discrepancy arises because atoms still undergo slowing as the field decays to zero outside of the

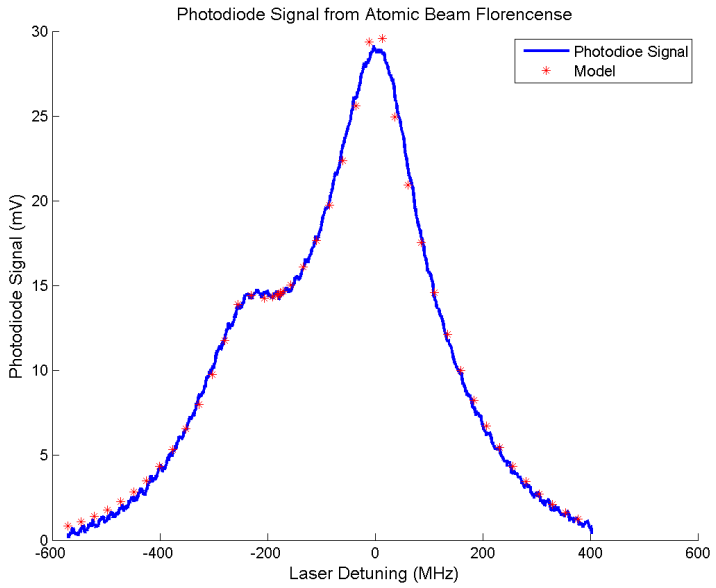


**Figure 4.6:** Fluorescence signal from a single probe beam transverse to the atomic beam at the output of the effusive source. The source was operated at 450°C.

slower. As the final velocity is tuned closer to zero, the peak disappears entirely indicating that the atoms have been turned around prior to reaching the probe beam. This problem has been reported in similar slower designs [29].

### 4.2.2 Assembling Experimental Apparatus and Bake-out

Prior to testing the slower by loading a MOT, the vacuum system must be assembled and baked out. In order to achieve the desirable base pressure, it is important that all components are clean. New parts are thoroughly cleaned by the manufacturer and are installed as is. Parts which have been previously used are sonicated in acetone for one hour, followed by methanol for one hour. Acetone is a stronger solvent than methanol, but tends to leave a residue. Parts which are machined are typically contaminated with oils and cooling fluids and must be cleaned more thoroughly. Such parts are hand washed with a mild detergent[1] and rinsed with water. They

[1]For our application, Simple Green All Purpose Cleaner is typically used.

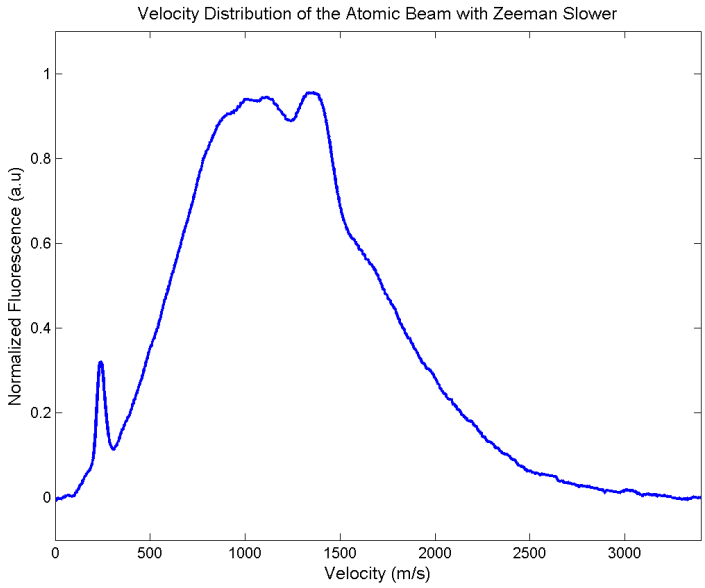


**Figure 4.7:** Velocity distribution of the lithium atomic beam when the slower is operational. The peak of slow atoms is centered at 240m/s

are then sonicated with the following solutions for a duration of one hour: (1) detergent, (2) distilled water, (3) acetone, and finally (4) methanol. The assembled apparatus is supported by an adjustable 8020 scaffolding and a temporary oven is erected from insulating fire bricks which is used for the bake-out. This can be seen in Figure 4.8.

### Loading Lithium

The lithium is stored in mineral oil which can easily contaminate the vacuum system. Therefore, the lithium oven is baked out separately from entire apparatus before being connected. Lithium oxides quickly and when exposed to air the surface will tarnish. The oxide layer can be easily removed with a razor blade, but will quickly form again in seconds when exposed to air. To prevent this, a clear garbage bag is filled with argon. The lithium is cut inside the bag and then transferred to the CF-nipple which is kept at positive argon pressure as well. All cutting tools are sonicated as well to minimize contamination. During the transfer process

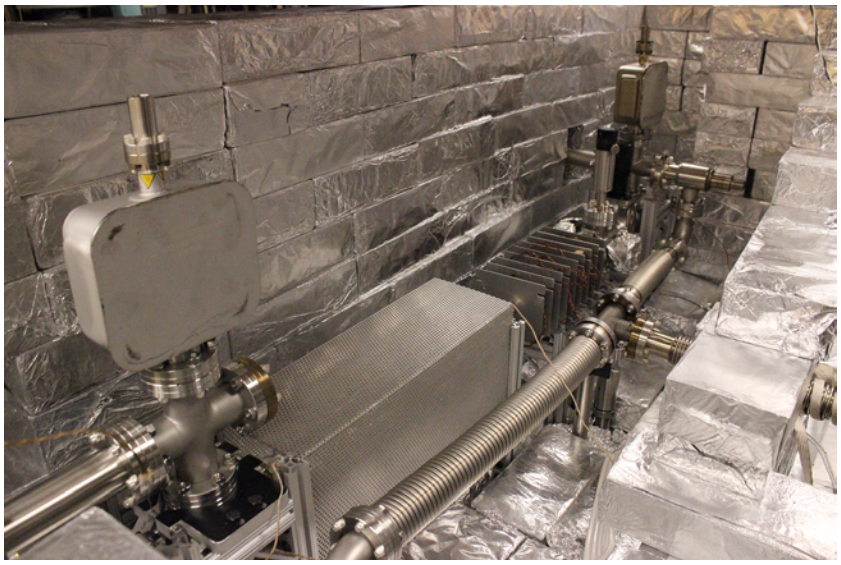

**Figure 4.8:** Experimental apparatus enclosed in the bake-out oven.

the lithium is sprayed by helium to prevent oxidization. Initially, we sprayed the lithium with nitrogen, but this lead to sample tarnishing presumably as result of forming a layer of LiN. The lithium was cooked at 500°C for 6 hours followed by 400°C for 12 hours. After cooling, the oven was back filled with argon and attached to main experimental apparatus. Figure 4.9 shows a RGA spectrum of the lithium loaded oven prior, during, and after the separate bake-out. We estimate that approximately 3g of isotope 6 enriched lithium was loaded into the oven.

### Bake-Out of Experimental Apparatus

As mentioned, the apparatus and lithium oven are initially baked out separately then attached for further baking. The first bake-out of the system was for 5 days at 185°C. The limiting factor for the temperature was the rotary feed through. One concern was that the coated wire for the Zeeman Slower would degrade and short after baking out. However, this was not an issue as the coating only darkened slightly during the bake-out. Figure 4.10 shows a residual gas analysis of the system prior, during, and after the first bake-out. During the first bake-out, the NEGS were activated which increased the hydrogen pressure of they system to $> 10^{-6}$

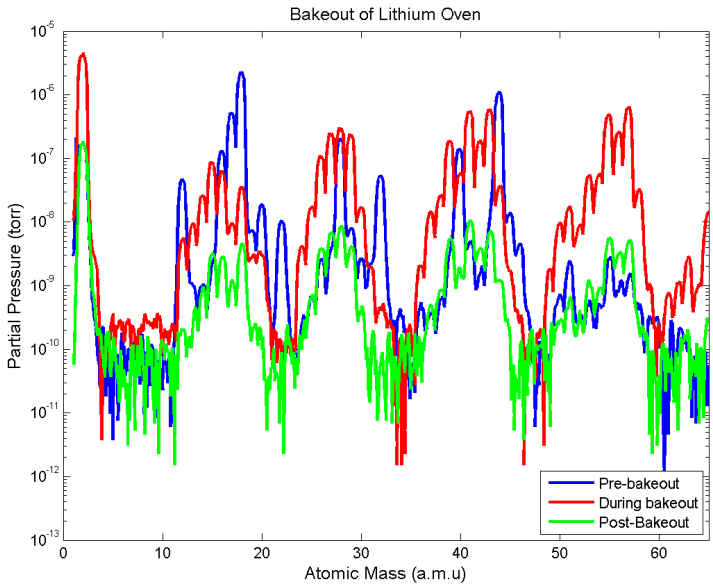


**Figure 4.9:** RGA trace of the lithium oven before, during, and after baking. The dominant contaminates are hydrogen (2amu), water (18amu), carbon monoxide (28 amu), and carbon dioxide (44 amu).

torr. Having the lithium separate at during this step help to prevent contamination by the large amount of hydrogen released during the activation.

After attaching the lithium, the system was baked following the same procedure as the first bake-out. Figure 4.11 shows a residual gas analysis of the system prior and after the second bake-out.

From the RGA traces, it is clear the largest contaminate in the system when the lithium is either hot or cold is hydrogen. Baking the lithium oven prior to connecting it to the apparatus helped eliminate the heavier species such as water, carbon monoxide, nitrogen and carbon dioxide, but did little to change the hydrogen base pressure. It is unclear what heating did to heavier species such as mineral oil as it is beyond the mass range of the RGA. Most likely, the large lithium sample loaded into the oven was completely saturated with hydrogen and trying to bake it all off is not feasible. Instead appropriate differential pumping and vacuum pumps must be installed in the apparatus.

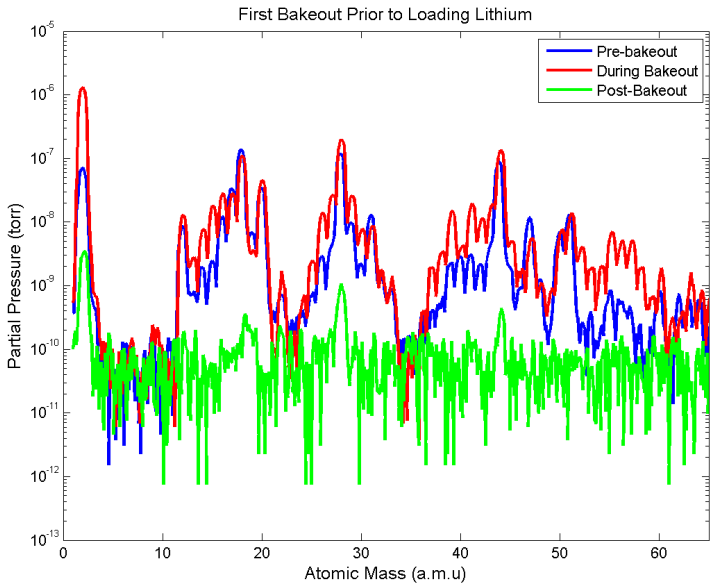


**Figure 4.10:** RGA trace of the vacuum system oven before, during, and after first bake-out.

### 4.2.3 Characterization with MOT

Upon completion of the bake out, the optics were setup for the dual lithium and rubidium MOT which was used to verify the final performance of the slower. The lithium and rubidium slowing beams are passed through a double pass AOM frequency shifter to allow for optimization of the detuning frequency before being combined with a long pass dichroic splitter. [2]. The slowing beam is expanded using a telescope such that is slowly comes to focus immediately before the slower. The benefit of this is two fold. First, the curvature of the slowing beam helps to focus the atomic beam and, secondly, the intensity at the MOT is less which helps to reduce the radiation pressure. The slowing beams are aligned down the optical axis by looking at the scattering off the shutter arm.

[2]Manufacturer: Edmond Optics Part, Number: #69 – 892

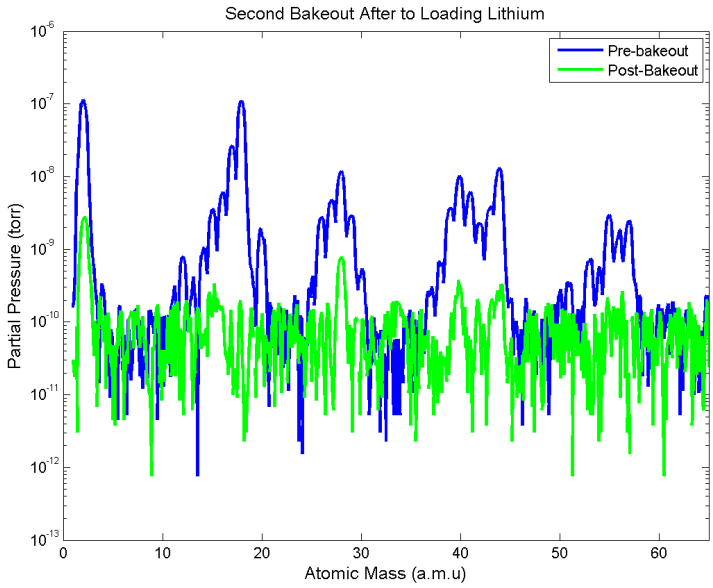


**Figure 4.11:** RGA trace of the vacuum system oven before and after the second bake-out.

### Lithium MOT

The lithium MOT was tested first with the Zeeman slower. In order for the Zeeman Slower to operate properly, the final coil had to be run backwards. In order for the Zeeman Slower to operate properly, the final coil had to be run backwards. This produced a rapidly decreasing magnetic field at the end of the slower whose gradient far exceeded the adiabatic condition thus disengaging the slowed atomic flux from the slowing beam thus preventing the atoms from being turned around by the slowing beam. The current in the last coil is optimized such that atoms leave the slower at a velocity which can be further slowed by the MOT field. If they are traveling too fast they will pass directly through the trap, while if they are moving to slowly, only a part of the full MOT field will be used for slowing. We observed that the slowing beam, without the Zeeman coils activated, also provided an increase in captured MOT flux. This was due to the MOT field extending outside of trapping region acting as a Zeeman slowing field. Loading curves for the MOT, MOT with slowing beam, and finally MOT with Zeeman Slower is shown in Figure 4.12. Be-

cause of delays in the code, the MOT starts loading approximately half a second before $t = 0$.

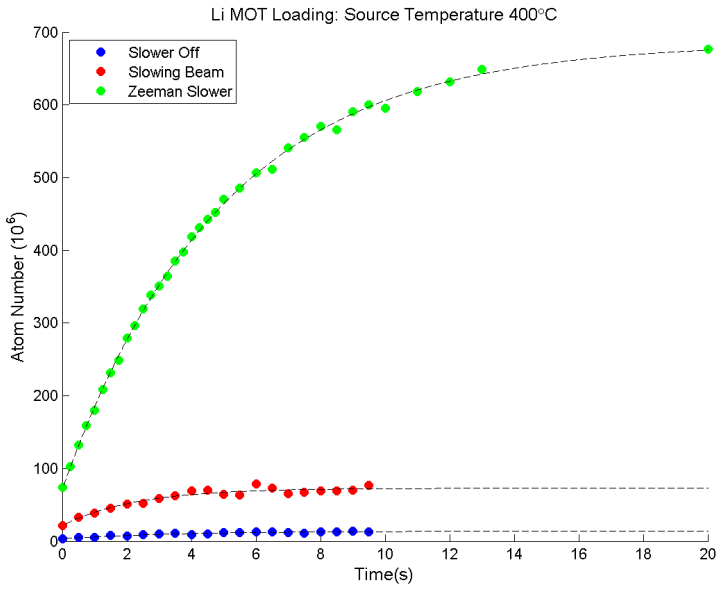


**Figure 4.12:** Loading curves for lithium MOT with and without the slower.

The a sequential optimization of all the Zeeman Slower currents was performed and all values agreed with that predicted by theory. The other MOT parameters are listed in Table 4.1. The detuning of both the pump and probe was also increased during the optimization of the Zeeman Slower. This did not affect the loading rate, but improved the MOT lifetime leading to larger steady state size.

The loading curves for the lithium MOT was fit to the following model.

$$N(t) = \frac{R}{\Gamma}(1 - \exp -t\Gamma) \tag{4.3}$$

where $N$ is the atom number, $R$ is the loading rate, and $\Gamma$ is the decay rate which is the inverse of the MOT lifetime [3]. The steady state atom number is given by $R/\Gamma$. The result of the fits is presented in Table 4.2.

[3] This equation is the solution to $\dot{N} = R - \Gamma N$

**Table 4.1:** Loading parameters for lithium MOT.

| Parameter | Value |
|---|---|
| Slowing Beam Detuning | -85 MHz |
| Slowing Beam Power | 45 mW |
| Pump Beam Detuning | -40 MHz |
| Repump Beam Detuning | -40 MHz |
| MOT Axial Gradient | 49 G/cm |
| Coil 1I | 6.7 A |
| Coil 2 I | 4.2 A |
| Coil 3 I | 3.28 A |
| Coil 4 I | 2.85 A |
| Coil 5 I | 2.52 A |
| Coil 6 I | 2.0 A |
| Coil 7 I | 1.74 A |
| Coil 8 I | -1.5 A |

**Table 4.2:** Lithium MOT loading curve fit values.

| Test | R ($10^6$ atoms/s) | Lifetime (s) | R/$\Gamma$ ($10^6$) |
|---|---|---|---|
| Only MOT | 4 | 3.5 | 14 |
| Slowing Beam | 32 | 2.2 | 72 |
| Zeeman Slower | 140 | 5.0 | 690 |

### Rubidium MOT

After the verifying the operation of Zeeman Slower for the lihtium slower, loading the rubiudm MOT was verified. Because of the mass difference, slowing rubdium is not as effective and a smaller field is needed. Rubidium exhibits much stronger saturation due to two body losses which limits the absolute size of the MOT. Therefore, the model which governs the loading of the rubidium MOT is given by Equation 4.4.

$$\frac{dN}{dt} = R - \Gamma N - \beta N^2 \tag{4.4}$$

where $\beta$ is the two body loss coefficient. The solution to Equation 4.4 whose solution is given by Equation 4.5.

$$N(t) = \frac{\sqrt{-4\beta R - \Gamma^2}\tan[\sqrt{-\beta R - (\Gamma/2)^2}(c_1 - t)] - \Gamma}{2\beta} \tag{4.5}$$

The parameter $c_1$ is arbitrary constant which sets the initial atom number. The loading curves for rubidium are shown in Figure 4.13 for cases when only the slowing beam on and when the Zeeman slower is on.

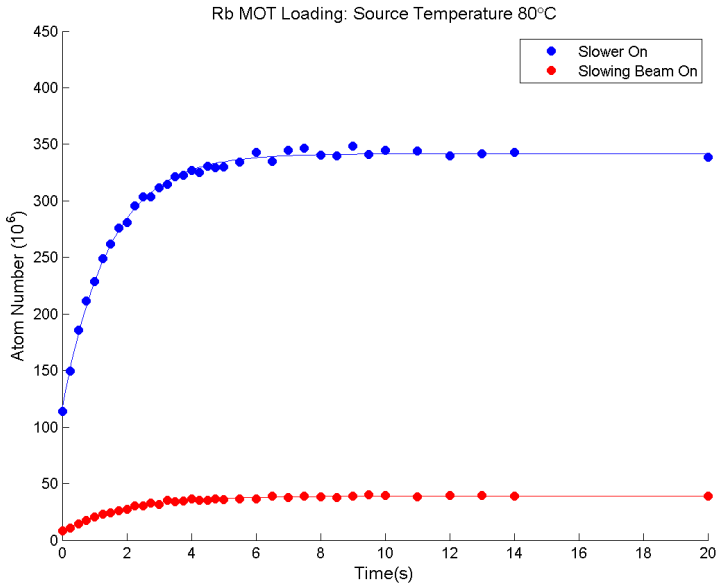


**Figure 4.13:** Loading curves for rubidium MOT with and without the slower.

The fit parameters for both curves are given in Table 4.3.

**Table 4.3:** Rubidium MOT loading curve fit values.

| Test | R ($10^6$ atoms/s) | Lifetime (s) | $N_{t=\infty}$ ($10^6$) | $\beta$ (atom· s)$^{-1}$ |
|---|---|---|---|---|
| Slowing Beam | 20 | 1.9 | 40 | – |
| Zeeman Slower | 232 | 1.5 | 350 | $2.1 \times 10^{-4}$ |

The MOT and Zeeman Slower setting used to load the MOT are given in Table 4.4.

**Table 4.4:** Loading parameters for rubidium MOT.

| Parameter | Value |
|---|---|
| Slowing Beam Detuning | -85 MHz |
| Slowing Beam Power | 15 mW |
| Slowing Repump Beam Detuning | 0 MHz |
| Slowing Repump Beam Power | 3 mW |
| Pump Beam Detuning | -18 MHz |
| Repump Beam Detuning | 0 |
| MOT Axial Gradient | 12.3 G/cm |
| Coil 1I | 0.85 A |
| Coil 2 I | 0.62 A |
| Coil 3 I | 0.52 A |
| Coil 4 I | 0.5 A |
| Coil 5 I | 0.4 A |
| Coil 6 I | 0.3 A |
| Coil 7 I | 0.3 A |
| Coil 8 I | -0.5 A |

### 4.2.4 Comparison of Observed and Simulated MOT Loading Rates

The model developed in Section 3.2 was compared the observed loading rates to determine its validity. For lithium, the model predicts a loading rate of $2.7 \times 10^8$ atoms per second at an operational temperature of 400°C, while the observed value was $1.4 \times 10^8$ at this temperature. The model predicts a rubidium loading rate of $8.0 \times 10^8$ atoms per second at an operational temperature of 80°C while the observed value is $2.4 \times 10^8$. The predicted flux is a factor of two higher for lithium and slightly more than three times larger for rubidium. Given the simplicity of the model, the agreement between the observed and simulated loading rates is very good. The model completely neglects optical pumping effects which would decrease the flux of cold atoms.

### 4.2.5 Improving Lithium MOT Lifetime

The atoms cooled in the MOT will be eventually transferred to a high power dipole trap. The dipole trap is shallower trap than the MOT and will therefore have a shorter lifetime. The duration of the evaporation in the dipole trap is typically be-

tween two and three seconds followed by any experiments which typically last for at most 1 second. Therefore, a reasonable upper bound for the dipole trap hold time is about is about 5s. In order to minimize atom loss during this process, the lifetime in the dipole trap should be at least 5s, but ideally closer to 10s. Because the background collision limited loss rate of the MOT (trap depth of 1K) is typically 5 times that of a shallow dipole trap (trap depth of less than 100 micro-Kelvin), the MOT lifetime should be between 60 to 100s to prevent significant atom loss during this hold time [34]. From the initial MOT loading, the lifetime is well below this target and must be improved by decreasing the pressure. The major contributor to background pressure is hydrogen which is measured to be $1.6 \times 10^{-9}$ torr. in the science chamber. In order to find the majority contributor to hydrogen the gate valve was closed which isolated the source and science sections. After pumping the system overnight while keeping the lithium at the operational temperature, the gate valve was reopened. The hydrogen pressure, as read by the RGA, only increased by 10% indicating that the source and science sections are well isolated by the differential pumping. Another possible culprit was the viewport for the slowing beam which is heated to prevent build up of lithium. Cooling the viewport to room temperature from 200°C decreased the hydrogen pressure down to $1 \times 10^{-9}$. This is alarming and indicated that the viewport or CF nipple to which it is attached could be contaminated. To investigate this possibility, a different CF flange was heated and pressure of hydrogen rose to $1.6 \times 10^{-9}$ torr. level indicating comparable out gassing. Loading curves were taken with and without the viewport heated to clearly show the effect of the improved vacuum on lifetime. The result is shown in Figure 4.14.
The result is fit to a model which includes two body losses as the loading curves exhibits saturation effects.

Finally, the effect of the atomic beam on MOT lifetime was investigated by blocking the atomic beam and looking at the decay in atom number. The result is shown is Figure 4.15. The data is fit to solution of Equation 4.4, but with $R$ set to zero. The MOT lifetime was the same with the beam blocked as unblocked and is thus unaffected by beam collisions. A summary of the tests is shown in the following Table 4.5.

Although the lifetime was improved, it still does not meet the required target.

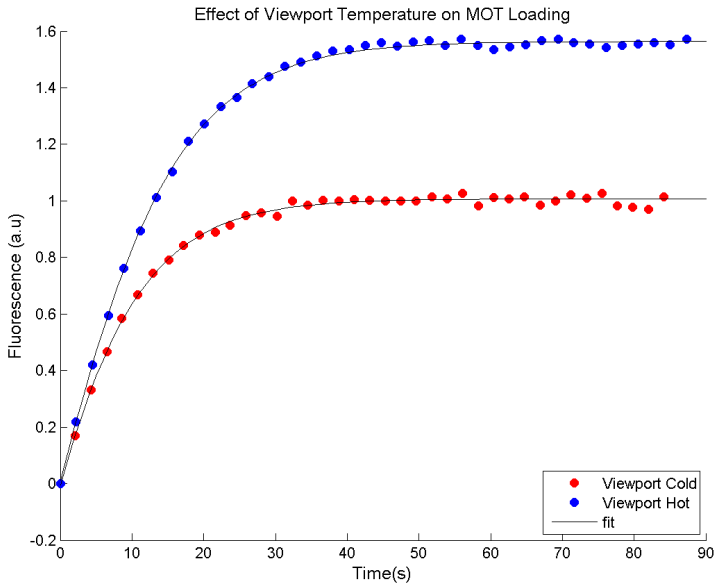


**Figure 4.14:** Effect of viewport temperature on MOT lifetime.

**Table 4.5:** Effect of viewport temperature and atomic beam on MOT lifetime.

| Test | Hydrogen Pressure ($10^{-}9$ torr.) | Lifetime (s) |
|---|---|---|
| Viewport Hot, MOT Loading | 1.6 | 15 |
| Viewport Cold, MOT Loading | 1 | 40 |
| Viewport Hot, MOT Loading | 1.6 | 15 |
| Viewport Cold, MOT Decay | 1 | 34 |

Improving differential pumping would not help as the source of hydrogen appears to be coming from the science side. Most likely another NEG must be added to the system.

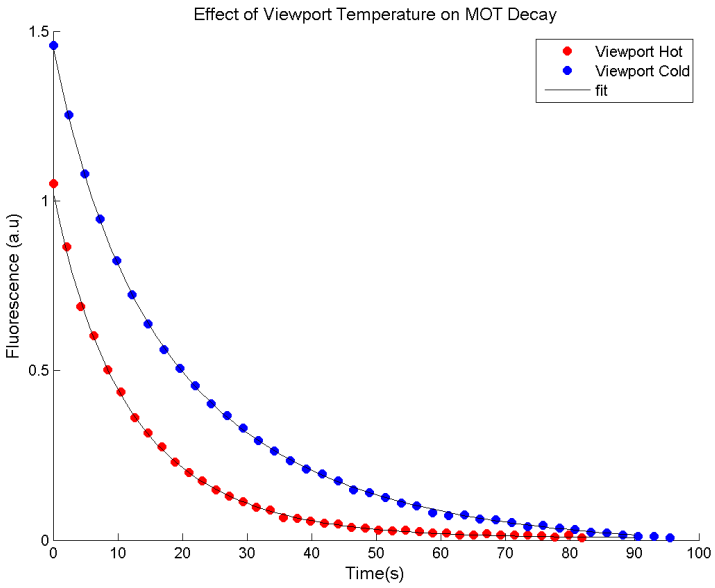


**Figure 4.15:** Effect of atomic beam on MOT lifetime.

# Chapter 5

# Conclusion and Future Work

We have presented the design, construction, and characterization of an experimental apparatus capable of producing cold samples of lithium and rubidium in a magneto-optical trap. This serves as a starting point for the study of ultracold mixtures and the formation of hetero-nuclear molecules. This thesis primarily focused on the design of a dual species effusive source and Zeeman slower. A physical model was developed to predict several of the operational parameters of the source such as flux, angular distribution, and velocity distribution. The model was compared to the experimental results which showed good agreement to the theory. The performance of the Zeeman slower was also tested by loading a MOT. The slower was capable of producing fluxes of cold atoms leading to loading rates in excess of $10^8$ atoms per second for both species. This was in reasonably good agreement with the model developed to predict the performance of the slower. Along with the performance of the slower, a detailed description of the vacuum system and magnetic field coils was also presented.

Moving forward, the main point in the design of the experimental apparatus which must be addressed in the short lifetime of atoms in the MOT due to the large background pressure of hydrogen. Currently, modifications to the system are underway to reduce the background pressure of hydrogen by adding additional differential pumping and installing another NEG between the slower and the trapping region.

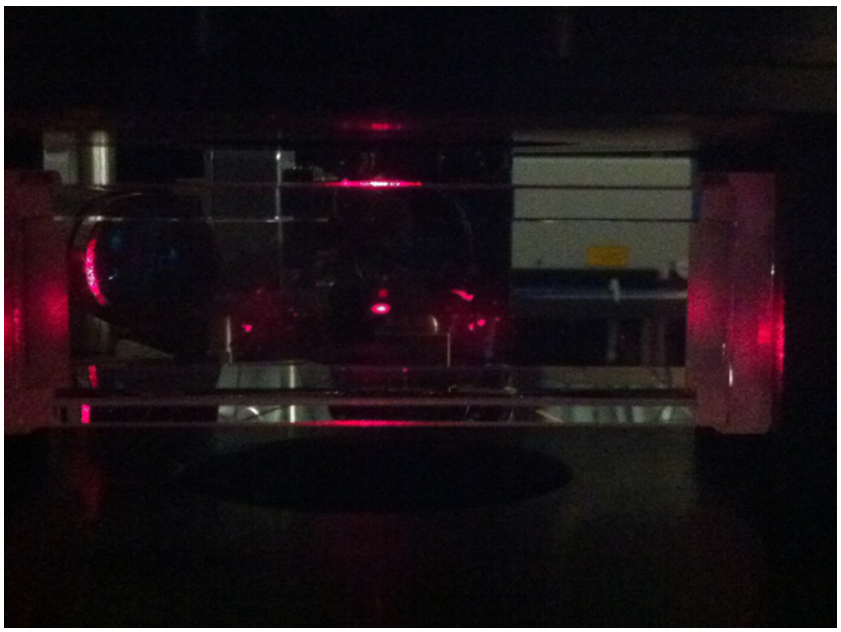

**Figure 5.1:** A lithium MOT with approximately half a billion atoms.

# Bibliography


[1] C. Ticknor and J. L. Bohn, "Long-range scattering resonances in strong-field-seeking states of polar molecules," *Phys. Rev. A*, vol. 72, p. 032717, Sep 2005. → pages 2

[2] A. V. Avdeenkov, D. C. E. Bortolotti, and J. L. Bohn, "Field-linked states of ultracold polar molecules," *Phys. Rev. A*, vol. 69, p. 012710, Jan 2004. → pages 2

[3] R. V. Krems, "Cold controlled chemistry," *Phys. Chem. Chem. Phys.*, vol. 10, pp. 4079–4092, 2008. → pages 2

[4] D. DeMille, "Quantum computation with trapped polar molecules," *Phys. Rev. Lett.*, vol. 88, p. 067901, Jan 2002. → pages 2

[5] S. F. Yelin, K. Kirby, and R. Côté, "Schemes for robust quantum computation with polar molecules," *Phys. Rev. A*, vol. 74, p. 050301, Nov 2006. → pages 2

[6] M. A. Baranov, "Theoretical progress in many-body physics with ultracold dipolar gases," *Physics Reports*, vol. 464, no. 3, pp. 71 – 111, 2008. → pages 2

[7] L. Santos, G. V. Shlyapnikov, P. Zoller, and M. Lewenstein, "Bose-einstein condensation in trapped dipolar gases," *Phys. Rev. Lett.*, vol. 85, pp. 1791–1794, Aug 2000. → pages 2

[8] M. Aymar and O. Dulieu, "Calculation of accurate permanent dipole moments of the lowest +1,3 states of heteronuclear alkali dimers using extended basis sets," *The Journal of Chemical Physics*, vol. 122, no. 20, 2005. → pages 2

[9] H. J. Metcalf and P. van der Straten, "Laser cooling and trapping of atoms," *J. Opt. Soc. Am. B*, vol. 20, pp. 887–908, May 2003. → pages 3

[10] D. A. Steck, "Rubidium 85 d line data." Online: http://steck.us/alkalidata/rubidium85numbers.pdf, 2008. An optional note. → pages 7

[11] M. E. Gehm, "Properties of 6li." Online:http://www.physics.ncsu.edu/jet/techdocs/pdf/PropertiesOfLi.pdf, 2003. An optional note. → pages 7

[12] E. Arimondo, M. Inguscio, and P. Violino, "Experimental determinations of the hyperfine structure in the alkali atoms," *Rev. Mod. Phys.*, vol. 49, pp. 31–75, Jan 1977. → pages 8

[13] A. Banerjee, A. Das, and V. Natarajan, "Absolute frequency measurements of the d 1 lines in 39 k, 85 rb, and 87 rb with 0.1 ppb uncertainty," *EPL (Europhysics Letters)*, vol. 65, no. 2, p. 172, 2004. → pages 8

[14] B. Ohayon and G. Ron, "New approaches in designing a zeeman slower," *Journal of Instrumentation*, vol. 8, no. 02, p. P02016, 2013. → pages 15

[15] E. Wille, *Preparation of an Optically Trapped Fermi-Fermi Mixture of 6Li and 40K Atoms and Characterization of the Interspecies Interactions by Feshbach Spectroscopy*. PhD thesis, Universitat Innsbruck, Innrain 52, 6020 Innsbruck, Austria, 2009. → pages 18

[16] W. Gunton, M. Semczuk, and K. W. Madison, "Realization of bec-bcs-crossover physics in a compact oven-loaded magneto-optic-trap apparatus," *Phys. Rev. A*, vol. 88, p. 023624, Aug 2013. → pages 19, 30

[17] K. Ladouceur, B. G. Klappauf, J. V. Dongen, N. Rauhut, B. Schuster, A. K. Mills, D. J. Jones, and K. W. Madison, "Compact laser cooling apparatus for simultaneous cooling of lithium and rubidium," *J. Opt. Soc. Am. B*, vol. 26, pp. 210–217, Feb 2009. → pages 19, 30

[18] C. A. Stan and W. Ketterle, "Multiple species atom source for laser-cooling experiments," *Review of Scientific Instruments*, vol. 76, no. 6, p. 063113, 2005. → pages 19

[19] N. Ramsey, *Molecular beams*. International series of monographs on physics, Clarendon Press, 1963. → pages 20, 21

[20] H. C. W. Beijerinck and N. F. Verster, "Velocity distribution and angular distribution of molecular beams from multichannel arrays," *Journal of Applied Physics*, vol. 46, no. 5, pp. 2083–2091, 1975. → pages 21, 22, 23

[21] P. Clausing, "The flow of highly rarefied gases through tubes of arbitrary length," *Journal of Vacuum Science and Technology*, vol. 8, no. 5, pp. 636–646, 1971. → pages 21, 22

[22] G. R. Hanes, "Multiple tube collimator for gas beams," *Journal of Applied Physics*, vol. 31, no. 12, pp. 2171–2175, 1960. → pages 23

[23] D. R. Olander, R. H. Jones, and W. J. Siekhaus, "Molecular beam sources fabricated from multichannel arrays. iv. speed distribution in the centerline beam," *Journal of Applied Physics*, vol. 41, no. 11, pp. 4388–4391, 1970. → pages 24, 25, 26

[24] L. Loeb, *The Kinetic Theory of Gases*. Dover Phoenix Editions, Dover Publications, 2004. → pages 25

[25] M. A. Joffe, W. Ketterle, A. Martin, and D. E. Pritchard, "Transverse cooling and deflection of an atomic beam inside a zeeman slower," *J. Opt. Soc. Am. B*, vol. 10, pp. 2257–2262, Dec 1993. → pages 33

[26] K. Gunter, "Design and implementation of a zeeman slower for 87rb," Master's thesis, Ecole Normale Superieure,, Paris, France, 2004. → pages 33

[27] U. Schnemann, H. Engler, M. Zielonkowski, M. Weidemller, and R. Grimm, "Magneto-optic trapping of lithium using semiconductor lasers," *Optics Communications*, vol. 158, no. 16, pp. 263 – 272, 1998. → pages 33

[28] S. C. Bell, M. Junker, M. Jasperse, L. D. Turner, Y.-J. Lin, I. B. Spielman, and R. E. Scholten, "A slow atom source using a collimated effusive oven and a single-layer variable pitch coil zeeman slower," *Review of Scientific Instruments*, vol. 81, no. 1, pp. –, 2010. → pages 34

[29] I. Kaldre, "A compact, air-cooled zeeman slower as a cold atom source," Master's thesis, Duke University, Durham, United States, 2006. → pages 35, 71

[30] P. Melentiev, P. Borisov, and V. Balykin, "Zeeman laser cooling of 85rb atoms in transverse magnetic field," *Journal of Experimental and Theoretical Physics*, vol. 98, no. 4, pp. 667–677, 2004. → pages 36

[31] T. Bergeman, G. Erez, and H. J. Metcalf, "Magnetostatic trapping fields for neutral atoms," *Phys. Rev. A*, vol. 35, pp. 1535–1546, Feb 1987. → pages 37

[32] S. Singh, "Progress towards ultra-cold ensembles of rubidium and lithium," Master's thesis, The University of British Columbia, Vancouver, Canada, 2007. → pages 65

[33] R. Senaratne, Z. Rajagopal, S.and Geiger, V. Fujiwara, K.; Lebedev, and D. Weld, "Effusive atomic oven nozzle design using a microcapillary array," *arXiv*, July 2014. → pages 66

[34] J. Van Dongen, C. Zhu, D. Clement, G. Dufour, J. L. Booth, and K. W. Madison, "Trap-depth determination from residual gas collisions," *Phys. Rev. A*, vol. 84, p. 022708, Aug 2011. → pages 81

# Appendix A

# Dampening Posts for Optical Bread Boards

The new experimental setup requires optical breadboards which sit adjacent to the experiment. These breadboards support sensitive optical components which are used for dipole traps and optical lattices and care should be taken to ensure they are stable. Inspired by commercially available posts which are designed to minimize dampening, we built custom posts. These posts use $80/20$ aluminum extrusions filled with lead shot to minimize vibrations. These posts are compared to standard $1''$ stainless steel posts which have been used previously to support bread boards.

Each post consists of a $80/20$ T-Slotted extrusion with dimensions $2'' \times 2'' \times 6''$. The extrusion has four holes which can be tapped for $1/4 - 20$ screws. These screws are used to secure the end caps made from $3/8''$ aluminum which are used to secure the post to the optical table and breadboard. Between the breadboard and endcap is a $1/16''$ cutout of nitrile rubber which acts as a spacer to further dampen vibrations. Prior to assembling the post, the inner cavity is filled with lead shot. In total, the entire post costs approximately $30 which is a third the price of a commercial post and clamp. The various parts of the post are shown in Figure A.1 prior to assembly.

In order to characterize the post's performance two breadboards were assembled with one being equipped with $1''$ Thorlabs posts and the other with our custom 8020 posts. In particular we were interested in two points: 1) how well isolated was

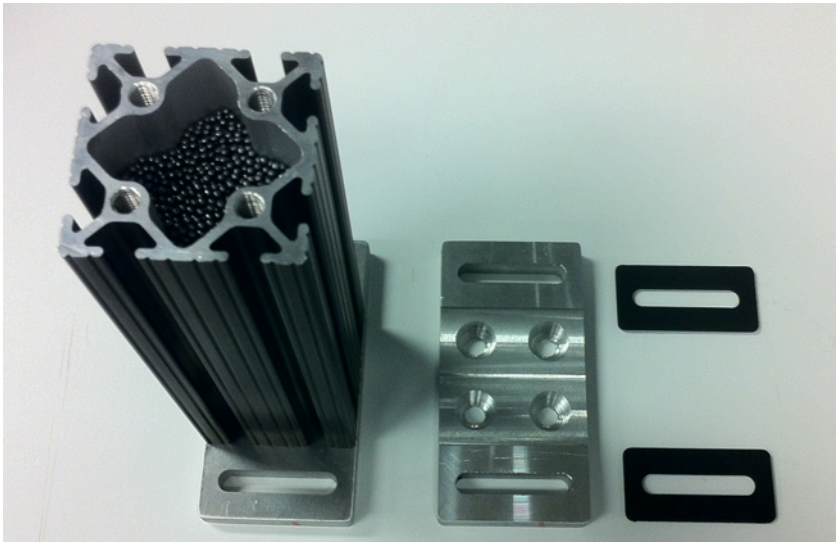

**Figure A.1:** The customs 80/20 post consist of a lead filled extrusion, identical top and bottom caps, and two nitrile spacers

the breadboard from the optical table and 2) how quickly were vibrations dampened once they coupled to the boardboard? In order to address these points we attached a peizoelectric accelerometer[1] to the breadboard and measured the impulse response to a disturbance on either the table or on the breadboard. In this case, the disturbance was a ball driver being dropped on the handle end from a fixed height as it reliably produced the same response. Figure A.2 is a plot showing the impulse response for disturbance on the optical table.

It is constructive to look at the Fourier transform of the two signals which clearly shows the improved frequency response. Unfortunately, the proportional calibration factor which related the voltage to acceleration is not known, however it is not needed for relative comparison of the two posts.

Next we dropped the ball driver directly on the breadboard. Once again, the custom posts are superior.

[1] model: 7703 manufacturer: ENDEVCO

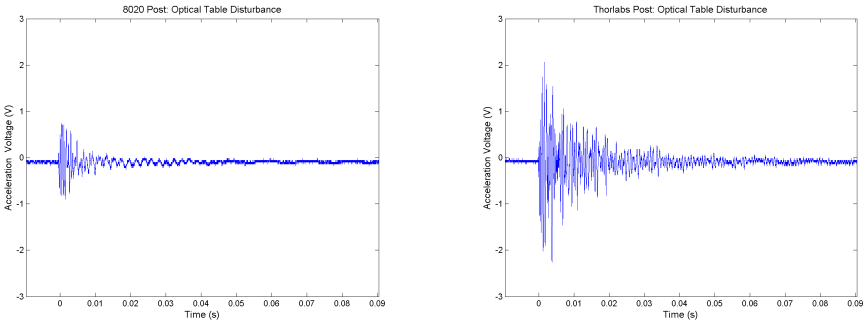


**(a)** 8020 Posts **(b)** Thorlabs Posts

**Figure A.2:** Impulse response of the breadboard to a disturbance on the optical table.

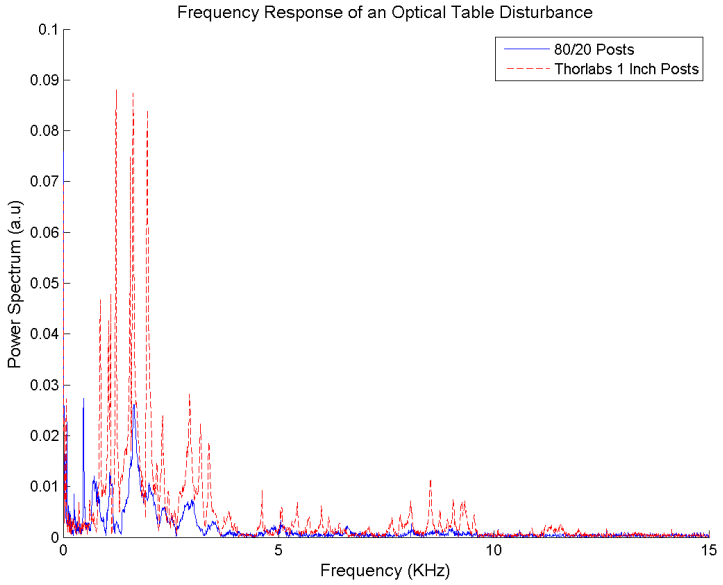


**Figure A.3:** Frequency response of the breadboard to a disturbance on the optical table.

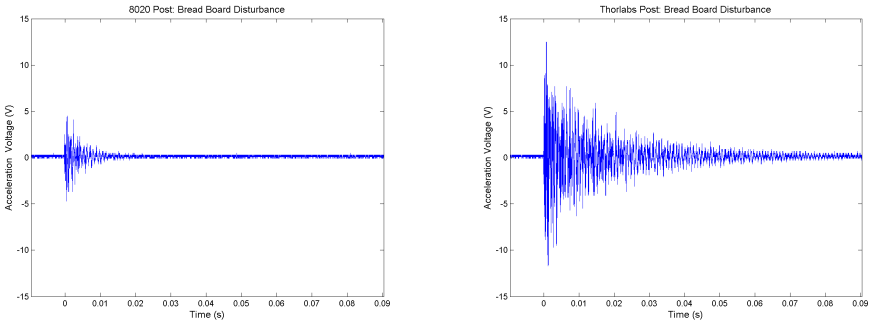


**(a)** 8020 Posts **(b)** Thorlabs Posts

**Figure A.4:** Impulse response of the breadboard to a disturbance on the breadboard directly.

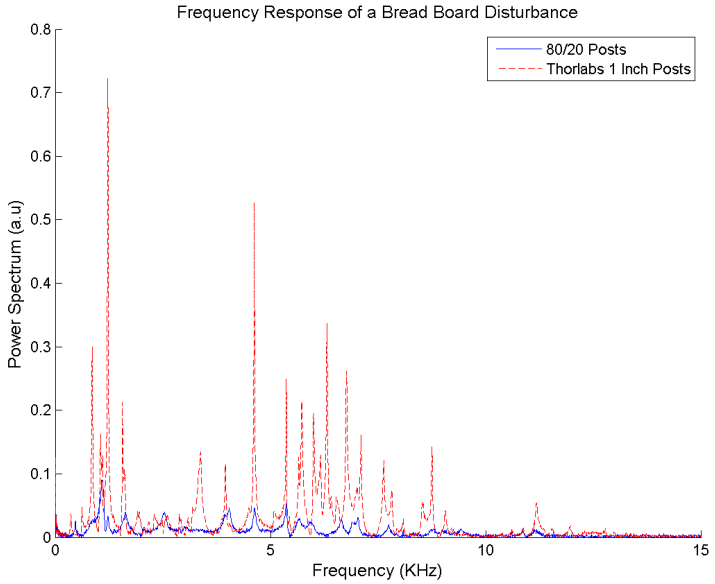


**Figure A.5:** Frequency response of the breadboard to a disturbance on the breadboard directly.

# Appendix B

# Measuring Dipole Trap Frequencies

## B.1 Introduction

Below is a brief summary on how to measure the trap frequency by modulating the power of the dipole trap laser (here called the "IPG"). **The power dependent transverse trap frequency was measured to be** $1.9kHz/\sqrt{W}$ **and the power dependent longitudinal trap frequency was measured to be** $0.13kHz/\sqrt{W}$**.**

## B.2 Setup

The RF power controlling the optical power diffracted towards the atoms with an AOM was modulated using a voltage controlled attenuator[1]. The control voltage input was attached to an adder circuit which combined a constant DC value of 10V with a sinusoid from a function generator [2]. The function generator was controlled using a USB port which was attached to the device via a USB to RS-232 converter. The sinusoid output was turned off and on by attaching a digital out port to the AM-Mod input on the back of the DS-345. For small sinusoid amplitudes, it was difficult to turn the signal completely off. Therefore, the output was attenuated

[1] manufacture: minicircuits model: ZX73-2500-S+

[2] manufacture: Stanford Instruments model: DS-345

by a 20-dbm attenuator before being attached to the adder. This allowed a larger amplitude to be set which could easily be shut off, while maintaining the correct modulation power.

The output of the DDS (the RF source generating 80 MHz) followed by the DDS-preamplifier was attached to the input of the RF attenuator, while the output was attached to the high power amplifier [3] **IMPORTANT: Do not exceed 10 dbm input power to the high power amplifier.** The amplifier power was compared with and without the attenuator. To compensate for the reduction in power by the attenuator, the output power from the first DDS was scaled by changing the attenuation factor in the code from 0.4 to 0.69.

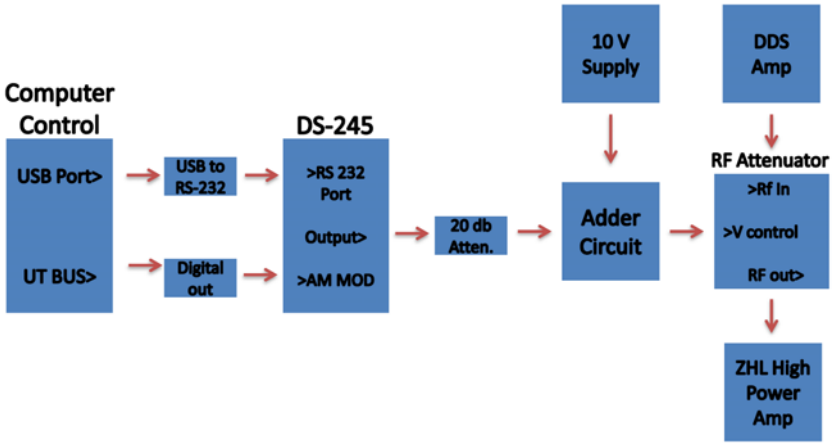


**Figure B.1:** Flow chart of measurement setup

## B.3 Experimental Method

It was found that the loss signal was greatly enhanced by having a three step excitation process. First the sample is cooled to an IPG power of 0.7 W (this corresponds to an IPG set power in the code of 0.5). Then the power increased adiabatically to the desired power (1 second ramp time). IIt was verified that when trapping lithium alone, the ratio of $T$ to $T_f$ did not change significantly during this stage. The IPG was then modulated at a given frequency for a fixed amplitude

[3] manufacture: minicircuits model: ZHL-03-SWF

and duration. It was observed that the attenuation level was frequency dependent for modulation frequency above 1 KHz. This is corrected for by dividing the desired function generator amplitude by a frequency dependent correction given by $C$=-0.0083713$f^2$+0.290178$f$+.77834. Finally, after the modulation the IPG power is ramped quickly (50ms) back to 0.7 W. The atom number is then measured as a function of modulation frequency to determine the resonance frequency of the trap. The strongest loss signal is observed at twice the trap resonance. A classical explanation follows from the fact if the trap is modulated at twice the frequency, the atoms are at the turning points during each field maximum and therefore experience the largest energy transfer.

## B.4 Experimental Parameters

The transverse frequency is much larger than the longitudinal frequency and shows a much clearer loss feature. The best signal was achieved by using relatively low excitation power and large modulation times. Below is a table summarizing the experimental parameters:

**Table B.1:** Experimental parameters for trap frequency measurements.

| Mode | Function Generator Amplitude (V) | Hold Time (s) |
|---|---|---|
| Transverse | 2 | 4 |
| Longitudinal | 4 | 8 |

## B.5 Results

Below are the standard loss spectra for various trap powers. All powers are the total trap power (i.e. the sum of both arms).

Fitting the peak location as a function of power gives the expected square root relation. These plots are shown below.

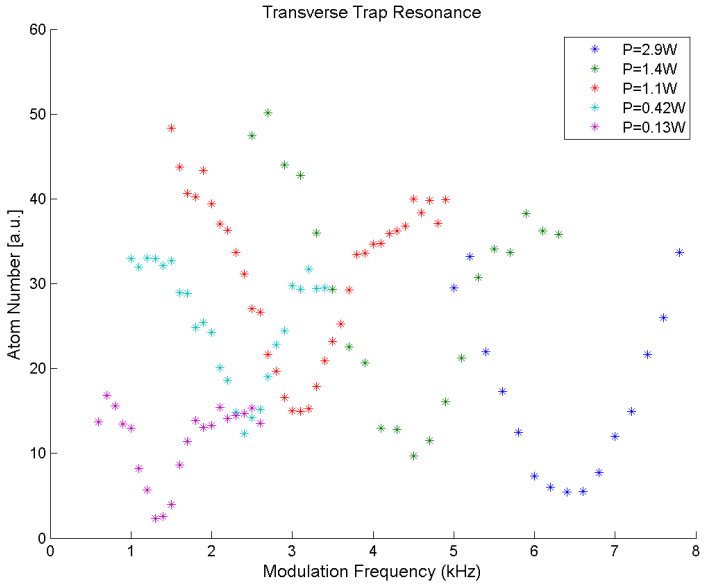


**Figure B.2:** Transverse frequency loss peaks.

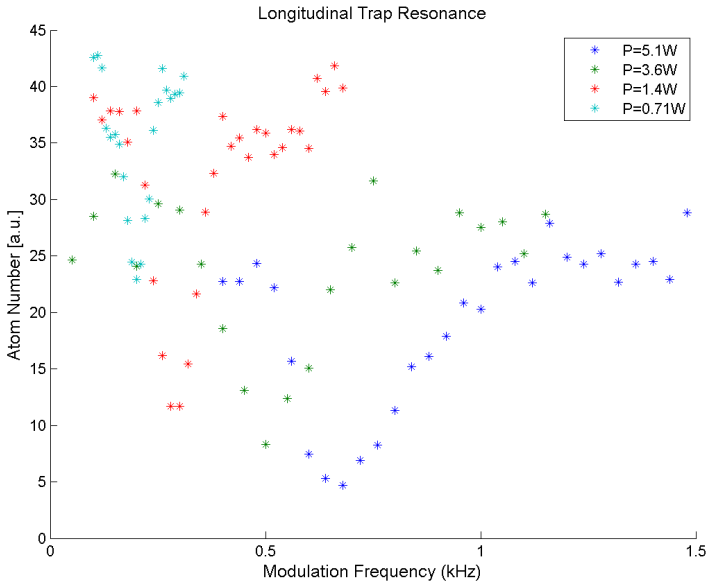


**Figure B.3:** Longitudinal frequency loss peaks.

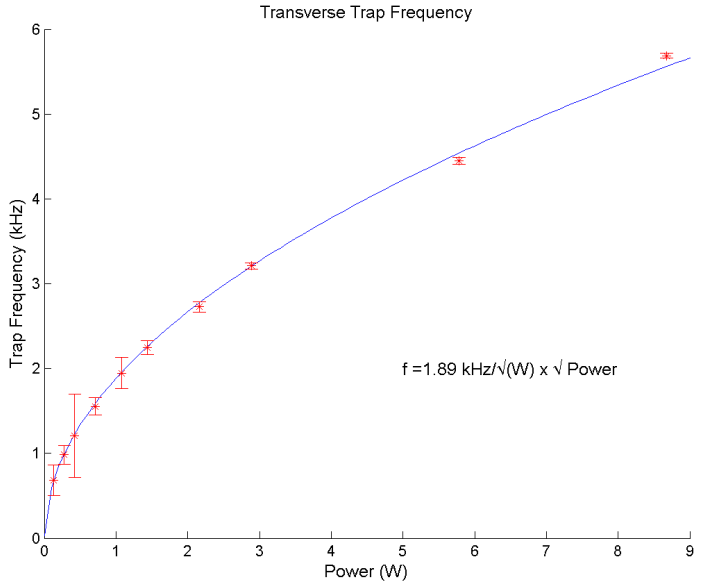


**Figure B.4:** Transverse frequency as a function of power.

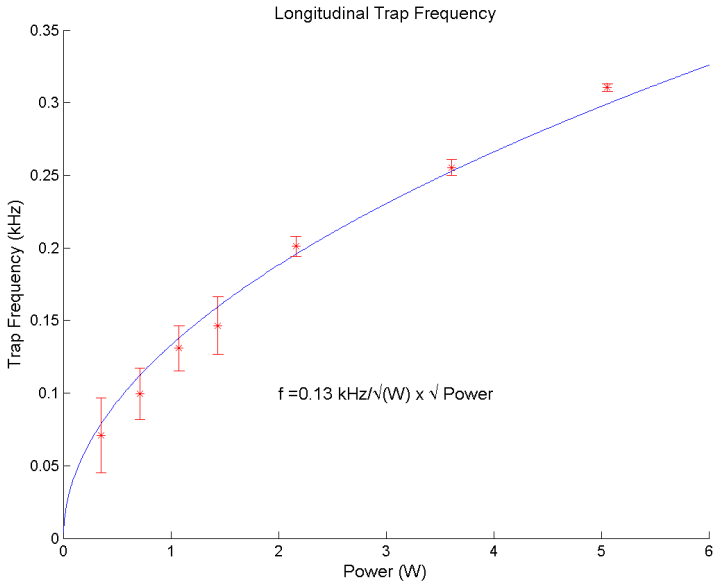


**Figure B.5:** Longitudinal frequency as a function of power.

# Appendix C

# Modeling Atomic Flux and Distribution from the Lithium Oven

Estimating the flux and angular distribution from an effusive source can be divided into two steps. The first step is to calculating the total florescence emitted from the atomic beam when excited by the probe beam. For this, the signal produced from the entire interaction length over which the atomic beam interacts with the probe must be integrated over. The florescence of each point along the probe is different for two reasons: (1) the local density of atoms is different due to the angular distribution from the source and (2) the Doppler shift is angle dependent. If the atomic beam is significantly dense or the probe beam is weak, one must take into account the abortion of the probe beam. The calculation is further complicated by the fact the atomic beam consists of many velocity classes, each of which experience a different Doppler shift. Therefore, the contribution of signal from each velocity class must also be integrated over.

The experimental apparatus is shown in Figure C.1. The coordinate $z$ denotes the distance along the probe beam with $z = 0$ being immediately in front of the source. The distance $d_1$ and $d_2$ are distances from $z = 0$ to the source and detector, respectively.

I will consider only a two-level system with natural linewidth $\gamma$, but the result

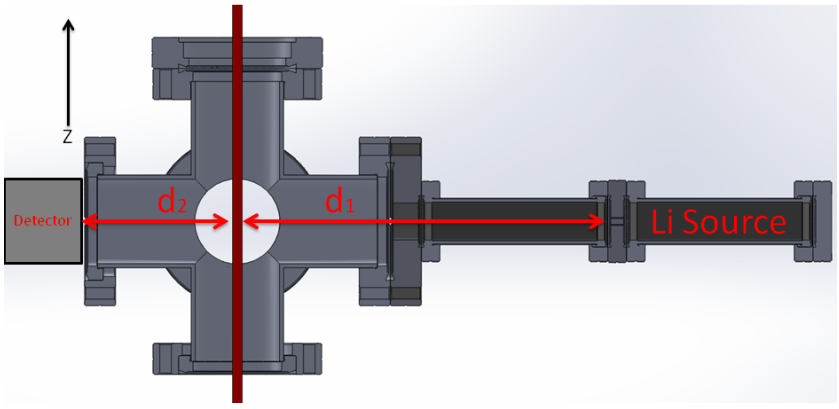


**Figure C.1:** Experimental setup used to characterize atomic beam.

can be easily extended to include the two hyperfine ground states of $Li_6$. The number of photons scattered, $ds$, from a length element between $z$ and $z+dz$ by atoms moving with speed between $v$ and $v+dv$ due to a probe beam with relative intensity $I/I_{sat}$ equal to $s_0$, cross sectional area $A$, and detuning $\delta$ is given by: [1]

$$\mathrm{ds}(\delta,z,v) = (n(z,v))\frac{\gamma}{2}\frac{s_0}{1+4(\frac{\delta+k\cdot v}{\gamma})^2}Adzdv \tag{C.1}$$

where n(z,v) is the local density of atoms at position $z$ moving with velocity $v$. Given the velocity distribution, $f(v)$ of atoms leaving the oven, given by Equation 2.31, and the angular distribution $g(\theta)$, given by Equation 2.36 and Equation 2.39, $n(z,v)$ can be calculated to be:

$$n(z,v) = N\frac{g(\theta)}{r^2 v}f(v) \tag{C.2}$$

where $N$ is the total number of atoms leaving the source and $r$ is the distance from the source to the element $dz$ on the probe beam given by:

$$d = \sqrt{z^2+d_1^2} \tag{C.3}$$

[1] This is only valid for the low intensity limit such that $s_0 \ll 1$, else the intensity distribution in the beam must be taken into account due to power broadening.

The Doppler shift as a function of position is given by:

$$k \cdot v = kv\sin\theta \tag{C.4}$$

where $\theta$ is the angle from the normal of the oven. The second part of the calculation is to determine what fraction of photons reach the photodiode and the power-to-voltage conversion factor of the detector which I denote as ($\alpha$). If the detector area, $A_d$ is small compared to the distance between the detector and probe beam then the fraction of photons captured ($F_c$) is simply given by:

$$F_c = \frac{A_d}{4\pi(d_2^2 + z^2)} \tag{C.5}$$

Hence, the voltage, $dV$, produced by the photodiode due to the scattering $ds$ is given by:

$$\mathrm{dV}(\delta) = \frac{\alpha \mathrm{ds}(\delta, z, v) A_d \mathrm{E}_{ph}}{4\pi(d_2^2 + z^2)} \tag{C.6}$$

where $\mathrm{E}_{ph}$ is the energy of the photon. Integrating over $z$ and $v$ gives the total voltage signal as function of detuning. The limits on the $z$ integral are typically defined by geometric constraints which limit the line of sight of the photodiode. The result of numerically integrating Equation C.6 is shown in Figure 4.6